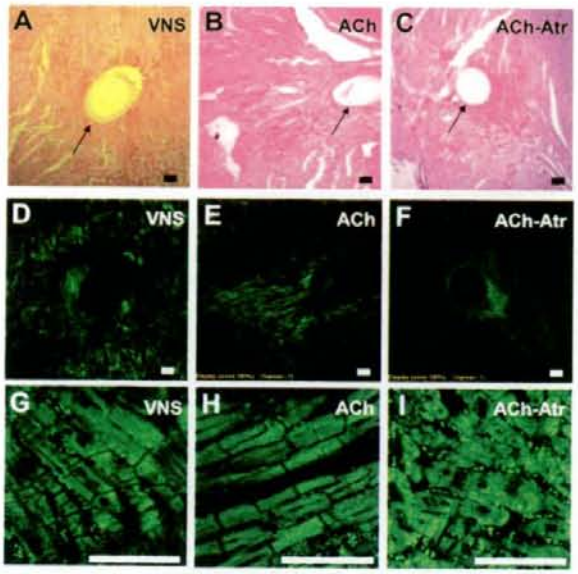

Fig. 5. Representative microscopic finding of left ventricular (LV) tissue implanted with microdialysis probe. *A–C*: hematoxylin and eosin-stained section of LV tissue perfused with Ringer solution under vagal nerve stimulation (VNS; *A*), perfused with ACh (*B*), and perfused with ACh and Atr (ACh-Atr; *C*). *D–F*: anti-TIMP-1 antibody (green)-immunostained sections of LV tissue perfused with Ringer solution under VNS (*D*), perfused with ACh (*E*), and perfused with ACh-Atr (*F*). *G–I*: higher magnifications of *D–F*, respectively. Arrows indicate dialysis probes. Bar = 100 μm.

myocardial ischemia are known to induce TIMP-1 (4). VNS and myocardial ischemia likely exerted an additive effect on the induction of TIMP-1 mRNA in the I/R-VS group. TIMP-1 protein levels in the VS and I/R-VS groups were significantly elevated compared with the sham and I/R groups (Fig. 3*A*). Figure 3, *A* and *C*, indicates dissociation between TIMP-1 mRNA and protein synthesis among the four groups. If the TIMP-1 protein level had correlated with the mRNA level, TIMP-1 protein level in the I/R and I/R-VS groups should have been higher than those presented in Fig. 3*A*. In myocardial ischemia, protein synthesis decreases owing to the inhibition of peptide chain elongation (8, 18). This may have partially inhibited TIMP-1 protein synthesis in the I/R and I/R-VS groups.

In the cardiac microdialysis study, the ACh-induced release of TIMP-1 was mediated by muscarinic ACh receptors because Atr blocked the increase in TIMP-1 in response to ACh stimulation (Fig. 4). TIMP-1 was produced by cardiomyocytes (Fig. 5, *G–I*). These findings suggest that VNS may induce TIMP-1 mRNA expression through muscarinic ACh receptors in cardiomyocytes and increase TIMP-1 protein content in myocardium. The distribution of TIMP-1-positive cardiomyocytes was different among the three groups (Fig. 5, *D–F*). This may reflect differences in the distribution of ACh among the three groups. ACh probably had a diffuse distribution in the myocardium in the VNS group but was concentrated around the dialysis probe in ACh group, whereas the effect of ACh concentrated around the dialysis probe was antagonized by Atr in the ACh-Atr group.

In addition to cardiomyocytes (25, 34), a variety of cell types, such as fibroblasts (14) and endothelial cells (6), produces and secretes TIMP-1. TIMP-1 expression in these cell types is low in the basal condition but is transcriptionally induced by various agents, including the cytokines, serum, growth factors, and phorbol esters (14). The signal transduction pathway from muscarinic ACh receptor stimulation to the induction of the TIMP-1 gene is not clear. Further elucidation of this is not in the scope of this study. ACh increases the production of nitric oxide from cardiomyocytes (9). Nitric oxide induces TIMP-1 gene expression by activating the transforming growth factor-β/Smad signaling pathway in glomerular mesangial cells in the kidney (2). These mechanisms may be involved in the increases in TIMP-1 mRNA and protein induced by VNS in myocardial I/R observed in the present study. Further studies are clearly required to elucidate these issues.

Myocardial expression of TIMP-2 was not modified by VNS (Fig. 3*B*). Contrary to the highly responsive nature of TIMP-1 expression to stimuli, TIMP-2 expression is, for the most part, constitutive (14). Previous studies demonstrated that ischemic injury or change in loading condition had little effect on myocardial expression of TIMP-2 (24, 25, 29). Myocardial content of MMP-2 decreased after I/R, and the decrease was inhibited by VNS (Fig. 1*C*). Cheung et al. (5) demonstrated that MMP-2 was released from the myocardium into the coronary effluent following myocardial I/R, resulting in the depletion of myocardial content of MMP-2.

In the present study, VNS did not prevent contractile dysfunction after I/R (Table 2). Actions of MMP and TIMP did not seem to be responsible for acute mechanical changes. Lu et al. (29) demonstrated that treatment with the MMP inhibitor failed to prevent acute myocardial dysfunction and regional expansion after I/R injury. The duration of reperfusion in our study (180 min) and that in Lu et al. (90 min) (29) may be too short to detect a significant influence of MMP and TIMP on regional LV function, which may become evident after a longer period of reperfusion.

Table 3. *Hemodynamic parameters during cardiac microdialysis study*

	Baseline	150 min
HR, beat/min		
VNS	286±7	227±7*†
ACh	303±16	308±9
ACh-Atr	304±14	298±16
MAP, mmHg		
VNS	101±8	103±8
ACh	93±3	100±4
ACh-Atr	87±3	92±6
LV dP/dt_{max}, mmHg/s		
VNS	5,050±588	4,768±475
ACh	5,203±345	5,488±400
ACh-Atr	4,519±269	4,718±450
FS, %		
VNS	7.4±1.8	7.2±1.9
ACh	5.0±1.2	4.9±1.2
ACh-Atr	5.4±0.5	5.0±0.5

Values are means ± SE. VNS group, LV tissue was perfused with Ringer solution via a dialysis probe under vagal nerve stimulation; ACh group, LV tissue was perfused with Ringer solution containing ACh (1 mM) via a dialysis probe; ACh-Atr group, LV tissue was perfused with ACh (1 mM) and atropine (0.2 mM) via a dialysis probe. *$P < 0.01$ vs. ACh; †$P < 0.01$ vs. ACh-Atr.

Several previous studies (10, 35, 39) demonstrated that targeted deletion of MMP-9 and/or the upregulation of TIMP-1 reduced infarct size, prevented LV rupture, and ameliorated LV remodeling after MI. Conversely, the expression of other MMPs, such as MMP-2, has been shown to be important in the myocardial healing that occurs in the later phases after ischemic injury (10). These observations suggest that the beneficial effect of VNS on LV remodeling after MI observed in our previous study (23) may be in a part mediated through the modified expression of MMPs and TIMPs as noted in the present study.

Except for the post-MI LV remodeling, MMPs and TIMPs contribute to the progression of various cardiovascular disorders, including expansion and rupture of aortic aneurysm (44), progression of acute viral myocarditis (15), and restenosis after coronary intervention (12). Local overexpression of TIMP-1 prevented the expansion and rupture of aortic aneurysm in rats (3) or prevented cardiac injury and dysfunction during experimental viral myocarditis in mice (15). VNS may be an effective biological inducer of TIMP-1 for the treatment of these disorders.

Limitation

The present study examined a limited number of MMP and TIMP species over a very short duration after myocardial I/R. A number of MMP and TIMP species are expressed in the myocardium, and several have been identified to be upregulated in cardiac disorders (24). Myocardial MMP-1 (collagenase) is induced by I/R (29). The actions of MMP-1 are inhibited in part by TIMP-1 (31). These suggest that VNS may inhibit the activity of MMP-1 in myocardial I/R injury. Further studies to define the effect of VNS on the profile of MMPs and TIMPs expressed in the myocardium are warranted.

In the present study, VNS was started 15 min before coronary occlusion. We did not examine whether VNS started after the coronary artery occlusion or whether reperfusion is capable of increasing myocardial TIMP-1. The pretreatment strategy as adopted in this study is unrealistic in clinical practice. Therefore, further studies are required to examine the time factor of VNS.

Concentration of ACh perfused through the dialysis probe in this study (1 mM) was substantially higher than the dialysate concentration of endogenous ACh released from the myocardium (<20 nM) (1). The ACh concentration within the myocardial interstitium might have been elevated over the supraphysiological range in the present microdialysis study. However, even if the interstitial concentration of ACh was unphysiologically high, Atr blocked the increase in TIMP-1 expression in response to ACh stimulation. Therefore, it is fair to say that TIMP-1 expression in response to ACh stimulation is mediated through the muscarinic ACh receptor.

TIMP-1 binds with MMPs to form a rather high molecular weight complex. Our preliminary in vitro experiment demonstrated that the relative recovery of TIMP-1/lipocalin/MMP-9 complex (Calbiochem, La Jolla, CA) was 3.8 ± 1.3% (range 0–5.5%) and was lower than that for free TIMP-1 (11.1 ± 0.3%) (see METHODS). Although the presence of MMPs, especially MMP-9, could affect the measurement of TIMP-1 within the myocardium by our microdialysis method, this probably does not affect the conclusion drawn from the cardiac microdialysis study, because the study was conducted in a heart free of I/R, which might contain low levels of myocardial MMP-9 as inferred from the results of the I/R study.

CONCLUSION

In a rabbit model of myocardial I/R injury, VNS induced TIMP-1 expression in cardiomyocytes and reduced active MMP-9.

GRANTS

This study was supported by a grant-in-aid for Scientific Research (C) (18500358) from the Ministry of Education, Culture, Sports, Science and Technology; by Health and Labour Sciences research grants for research on medical devices for analyzing, supporting and substituting the function of human body (H15-physi-001) from the Ministry of Health, Labour and Welfare of Japan; and by a research grant from the Fukuda Foundation for Medical Technology.

REFERENCES

1. **Akiyama T, Yamazaki T.** Adrenergic inhibition of endogenous acetylcholine release on postganglionic cardiac vagal nerve terminals. *Cardiovasc Res* 46: 531–538, 2000.
2. **Akool el-S, Doller A, Muller R, Gutwein P, Xin C, Huwiler A, Pfeilschifter J, Eberhardt W.** Nitric oxide induces TIMP-1 expression by activating the transforming growth factor beta-Smad signaling pathway. *J Biol Chem* 280: 39403–39416, 2005.
3. **Allaire E, Forough R, Clowes M, Starcher B, Clowes AW.** Local overexpression of TIMP-1 prevents aortic aneurysm degeneration and rupture in a rat model. *J Clin Invest* 102: 1413–1420, 1998.
4. **Chandrasekar B, Smith JB, Freeman GL.** Ischemia-reperfusion of rat myocardium activates nuclear factor-KappaB and induces neutrophil infiltration via lipopolysaccharide-induced CXC chemokine. *Circulation* 103: 2296–2302, 2001.
5. **Cheung PY, Sawicki G, Wozniak M, Wang W, Radomski MW, Schulz R.** Matrix metalloproteinase-2 contributes to ischemia-reperfusion injury in the heart. *Circulation* 101: 1833–1839, 2000.
6. **Chua CC, Hamdy RC, Chua BH.** Angiotensin II induces TIMP-1 production in rat heart endothelial cells. *Biochim Biophys Acta* 1311: 175–180, 1996.
7. **Chua PK, Melish ME, Yu Q, Yanagihara R, Yamamoto KS, Nerurkar VR.** Elevated levels of matrix metalloproteinase 9 and tissue inhibitor of metalloproteinase 1 during the acute phase of Kawasaki disease. *Clin Diagn Lab Immunol* 10: 308–314, 2003.
8. **Crozier SJ, Vary TC, Kimball SR, Jefferson LS.** Cellular energy status modulates translational control mechanisms in ischemic-reperfused rat hearts. *Am J Physiol Heart Circ Physiol* 289: H1242–H1250, 2005.
9. **Dedkova EN, Ji X, Wang YG, Blatter LA, Lipsius SL.** Signaling mechanisms that mediate nitric oxide production induced by acetylcholine exposure and withdrawal in cat atrial myocytes. *Circ Res* 93: 1233–1240, 2003.
10. **Ducharme A, Frantz S, Aikawa M, Rabkin E, Lindsey M, Rohde LE, Schoen FJ, Kelly RA, Werb Z, Libby P, Lee RT.** Targeted deletion of matrix metalloproteinase-9 attenuates left ventricular enlargement and collagen accumulation after experimental myocardial infarction. *J Clin Invest* 106: 55–62, 2000.
11. **Ergul A, Walker CA, Goldberg A, Baicu SC, Hendrick JW, King MK, Spinale FG.** ET-1 in the myocardial interstitium: relation to myocyte ECE activity and expression. *Am J Physiol Heart Circ Physiol* 278: H2050–H2056, 2000.
12. **Feldman LJ, Mazighi M, Scheuble A, Deux JF, De Benedetti E, Badier-Commander C, Brambilla E, Henin D, Steg PG, Jacob MP.** Differential expression of matrix metalloproteinases after stent implantation and balloon angioplasty in the hypercholesterolemic rabbit. *Circulation* 103: 3117–3122, 2001.
13. **Fujimoto N, Zhang J, Iwata K, Shinya T, Okada Y, Hayakawa T.** A one-step sandwich enzyme immunoassay for tissue inhibitor of metalloproteinases-2 using monoclonal antibodies. *Clin Chim Acta* 220: 31–45, 1993.
14. **Gomez DE, Alonso DF, Yoshiji H, Thorgeirsson UP.** Tissue inhibitors of metalloproteinases: structure, regulation and biological functions. *Eur J Cell Biol* 74: 111–122, 1997.

15. **Heymans S, Pauschinger M, De Palma A, Kallwellis-Opara A, Rutschow S, Swinnen M, Vanhoutte D, Gao F, Torpai R, Baker AH, Padalko E, Neyts J, Schultheiss HP, Van de Werf F, Carmeliet P, Pinto YM.** Inhibition of urokinase-type plasminogen activator or matrix metalloproteinases prevents cardiac injury and dysfunction during viral myocarditis. *Circulation* 114: 565–573, 2006.
16. **Hudson MP, Armstrong PW, Ruzyllo W, Brum J, Cusmano L, Krzeski P, Lyon R, Quinones M, Theroux P, Sydlowski D, Kim HE, Garcia MJ, Jaber WA, Weaver WD.** Effects of selective matrix metalloproteinase inhibitor (PG-116800) to prevent ventricular remodeling after myocardial infarction: results of the PREMIER (Prevention of Myocardial Infarction Early Remodeling) trial. *J Am Coll Cardiol* 48: 15–20, 2006.
17. **Kameda K, Matsunaga T, Abe N, Hanada H, Ishizaka H, Ono H, Saitoh M, Fukui K, Fukuda I, Osanai T, Okumura K.** Correlation of oxidative stress with activity of matrix metalloproteinase in patients with coronary artery disease. Possible role for left ventricular remodelling. *Eur Heart J* 24: 2180–2185, 2003.
18. **Kao R, Rannels DE, Morgan HE.** Effects of anoxia and ischemia on protein synthesis in perfused rat hearts. *Circ Res* 38, *Suppl* 1: I124–I130, 1976.
19. **Kitagawa H, Yamazaki T, Akiyama T, Sugimachi M, Sunagawa K, Mori H.** Microdialysis separately monitors myocardial interstitial myoglobin during ischemia and reperfusion. *Am J Physiol Heart Circ Physiol* 289: H924–H930, 2005.
20. **Kodama S, Iwata K, Iwata H, Yamashita K, Hayakawa T.** Rapid one-step sandwich enzyme immunoassay for tissue inhibitor of metalloproteinases. An application for rheumatoid arthritis serum and plasma. *J Immunol Methods* 127: 103–108, 1990.
21. **La Rovere MT, Bigger JT Jr, Marcus FI, Mortara A, Schwartz PJ.** Baroreflex sensitivity and heart-rate variability in prediction of total cardiac mortality after myocardial infarction. ATRAMI (Autonomic Tone and Reflexes After Myocardial Infarction) Investigators. *Lancet* 351: 478–484, 1998.
22. **Le Quellec A, Dupin S, Genissel P, Saivin S, Marchand B, Houin G.** Microdialysis probes calibration: gradient and tissue dependent changes in no net flux and reverse dialysis methods. *J Pharmacol Toxicol Methods* 33: 11–16, 1995.
23. **Li M, Zheng C, Sato T, Kawada T, Sugimachi M, Sunagawa K.** Vagal nerve stimulation markedly improves long-term survival after chronic heart failure in rats. *Circulation* 109: 120–124, 2004.
24. **Li YY, Feldman AM, Sun Y, McTiernan CF.** Differential expression of tissue inhibitors of metalloproteinases in the failing human heart. *Circulation* 98: 1728–1734, 1998.
25. **Li YY, Feng Y, McTiernan CF, Pei W, Moravec CS, Wang P, Rosenblum W, Kormos RL, Feldman AM.** Downregulation of matrix metalloproteinases and reduction in collagen damage in the failing human heart after support with left ventricular assist devices. *Circulation* 104: I147–I152, 2001.
26. **Lindsey M, Wedin K, Brown MD, Keller C, Evans AJ, Smolen J, Burns AR, Rossen RD, Michael L, Entman M.** Matrix-dependent mechanism of neutrophil-mediated release and activation of matrix metalloproteinase 9 in myocardial ischemia/reperfusion. *Circulation* 103: 2181–2187, 2001.
27. **Lindsey ML, Gannon J, Aikawa M, Schoen FJ, Rabkin E, Lopresti-Morrow L, Crawford J, Black S, Libby P, Mitchell PG, Lee RT.** Selective matrix metalloproteinase inhibition reduces left ventricular remodeling but does not inhibit angiogenesis after myocardial infarction. *Circulation* 105: 753–758, 2002.
28. **Livak KJ, Schmittgen TD.** Analysis of relative expression data using real-time quantitative PCR and the $2^{-\Delta\Delta C_T}$ method. *Methods* 25: 402–408, 2001.
29. **Lu L, Gunja-Smith Z, Woessner JF, Ursell PC, Nissen T, Galardy RE, Xu Y, Zhu P, Schwartz GG.** Matrix metalloproteinases and collagen ultrastructure in moderate myocardial ischemia and reperfusion in vivo. *Am J Physiol Heart Circ Physiol* 279: H601–H609, 2000.
30. **Mioni C, Bazzani C, Giuliani D, Altavilla D, Leone S, Ferrari A, Minutoli L, Bitto A, Marini H, Zaffe D, Botticelli AR, Iannone A, Tomasi A, Bigiani A, Bertolini A, Squadrito F, Guarini S.** Activation of an efferent cholinergic pathway produces strong protection against myocardial ischemia/reperfusion injury in rats. *Crit Care Med* 33: 2621–2628, 2005.
31. **Moe SM, Singh GK, Bailey AM.** Beta2-microglobulin induces MMP-1 but not TIMP-1 expression in human synovial fibroblasts. *Kidney Int* 57: 2023–2034, 2000.
32. **Mukherjee R, Brinsa TA, Dowdy KB, Scott AA, Baskin JM, Deschamps AM, Lowry AS, Escobar GP, Lucas DG, Yarbrough WM, Zile MR, Spinale FG.** Myocardial infarct expansion and matrix metalloproteinase inhibition. *Circulation* 107: 618–625, 2003.
33. **Pfeffer MA, Braunwald E.** Ventricular remodeling after myocardial infarction. Experimental observations and clinical implications. *Circulation* 81: 1161–1172, 1990.
34. **Romanic AM, Burns-Kurtis CL, Gout B, Berrebi-Bertrand I, Ohlstein EH.** Matrix metalloproteinase expression in cardiac myocytes following myocardial infarction in the rabbit. *Life Sci* 68: 799–814, 2001.
35. **Romanic AM, Harrison SM, Bao W, Burns-Kurtis CL, Pickering S, Gu J, Grau E, Mao J, Sathe GM, Ohlstein EH, Yue TL.** Myocardial protection from ischemia/reperfusion injury by targeted deletion of matrix metalloproteinase-9. *Cardiovasc Res* 54: 549–558, 2002.
36. **Silvestry SC, Taylor DA, Lilly RE, Atkins BZ, Marathe US, Davis JW, Kraus W, Glower DD.** The in vivo quantification of myocardial performance in rabbits: a model for evaluation of cardiac gene therapy. *J Mol Cell Cardiol* 28: 815–823, 1996.
37. **Squire IB, Evans J, Ng LL, Loftus IM, Thompson MM.** Plasma MMP-9 and MMP-2 following acute myocardial infarction in man: correlation with echocardiographic and neurohumoral parameters of left ventricular dysfunction. *J Card Fail* 10: 328–333, 2004.
38. **Stapel H, Kim SC, Osterkamp S, Knuefermann P, Hoeft A, Meyer R, Grohe C, Baumgarten G.** Toll-like receptor 4 modulates myocardial ischaemia-reperfusion injury: role of matrix metalloproteinases. *Eur J Heart Fail* 8: 665–672, 2006.
39. **Trescher K, Bernecker O, Fellner B, Gyongyosi M, Schafer R, Aharinejad S, DeMartin R, Wolner E, Podesser BK.** Inflammation and postinfarct remodeling: overexpression of IkappaB prevents ventricular dilation via increasing TIMP levels. *Cardiovasc Res* 69: 746–754, 2006.
40. **Udelson JE, Konstam MA.** Relation between left ventricular remodeling and clinical outcomes in heart failure patients with left ventricular systolic dysfunction. *J Card Fail* 8: S465–S471, 2002.
41. **Uemura S, Matsushita H, Li W, Glassford AJ, Asagami T, Lee KH, Harrison DG, Tsao PS.** Diabetes mellitus enhances vascular matrix metalloproteinase activity: role of oxidative stress. *Circ Res* 88: 1291–1298, 2001.
42. **Verheijen JH, Nieuwenbroek NM, Beekman B, Hanemaaijer R, Verspaget HW, Ronday HK, Bakker AH.** Modified proenzymes as artificial substrates for proteolytic enzymes: colorimetric assay of bacterial collagenase and matrix metalloproteinase activity using modified prourokinase. *Biochem J* 323: 603–609, 1997.
43. **Webb CS, Bonnema DD, Ahmed SH, Leonardi AH, McClure CD, Clark LL, Stroud RE, Corn WC, Finklea L, Zile MR, Spinale FG.** Specific temporal profile of matrix metalloproteinase release occurs in patients after myocardial infarction: relation to left ventricular remodeling. *Circulation* 114: 1020–1027, 2006.
44. **Wilson WR, Anderton M, Schwalbe EC, Jones JL, Furness PN, Bell PR, Thompson MM.** Matrix metalloproteinase-8 and -9 are increased at the site of abdominal aortic aneurysm rupture. *Circulation* 113: 438–445, 2006.
45. **Winer J, Jung CK, Shackel I, Williams PM.** Development and validation of real-time quantitative reverse transcriptase-polymerase chain reaction for monitoring gene expression in cardiac myocytes in vitro. *Anal Biochem* 270: 41–49, 1999.

Am J Physiol Heart Circ Physiol 293: H1564–H1570, 2007.
First published May 25, 2007; doi:10.1152/ajpheart.00368.2007.

Muscarinic potassium channels augment dynamic and static heart rate responses to vagal stimulation

Masaki Mizuno,[1] Atsunori Kamiya,[1] Toru Kawada,[1] Tadayoshi Miyamoto,[1,2,3] Shuji Shimizu,[1,2] and Masaru Sugimachi[1]

[1]*Department of Cardiovascular Dynamics, Advanced Medical Engineering Center, National Cardiovascular Center Research Institute, and* [3]*Morinomiya University of Medical Sciences, Osaka; and* [2]*Japan Association for the Advancement of Medical Equipment, Tokyo, Japan*

Submitted 23 March 2007; accepted in final form 22 May 2007

Mizuno M, Kamiya A, Kawada T, Miyamoto T, Shimizu S, Sugimachi M. Muscarinic potassium channels augment dynamic and static heart rate responses to vagal stimulation. *Am J Physiol Heart Circ Physiol* 293: H1564–H1570, 2007. First published May 25, 2007; doi:10.1152/ajpheart.00368.2007.—Vagal control of heart rate (HR) is mediated by direct and indirect actions of ACh. Direct action of ACh activates the muscarinic K^+ (K_{ACh}) channels, whereas indirect action inhibits adenylyl cyclase. The role of the K_{ACh} channels in the overall picture of vagal HR control remains to be elucidated. We examined the role of the K_{ACh} channels in the transfer characteristics of the HR response to vagal stimulation. In nine anesthetized sinoaortic-denerved and vagotomized rabbits, the vagal nerve was stimulated with a binary white-noise signal (0–10 Hz) for examination of the dynamic characteristic and in a step-wise manner (5, 10, 15, and 20 Hz/min) for examination of the static characteristic. The dynamic transfer function from vagal stimulation to HR approximated a first-order, low-pass filter with a lag time. Tertiapin, a selective K_{ACh} channel blocker (30 nmol/kg iv), significantly decreased the dynamic gain from 5.0 ± 1.2 to 2.0 ± 0.6 (mean ± SD) beats·min^{-1}·Hz^{-1} ($P < 0.01$) and the corner frequency from 0.25 ± 0.03 to 0.06 ± 0.01 Hz ($P < 0.01$) without changing the lag time (0.37 ± 0.04 vs. 0.39 ± 0.05 s). Moreover, tertiapin significantly attenuated the vagal stimulation-induced HR decrease by 46 ± 21, 58 ± 18, 65 ± 15, and 68 ± 11% at stimulus frequencies of 5, 10, 15, and 20 Hz, respectively. We conclude that K_{ACh} channels contribute to a rapid HR change and to a larger decrease in the steady-state HR in response to more potent tonic vagal stimulation.

systems analysis; transfer function; muscarinic receptor; rabbit

VAGAL CONTROL OF HEART RATE (HR) is mediated by a cascade reaction to ACh release. ACh binds to M_2 muscarinic receptors and, consequently, decreases HR. However, the pathway is not simple; two different pathways mediate the ACh-induced HR decrease. The M_2 muscarinic receptors activate heterotrimeric G_i and/or G_o proteins in cardiac myocytes (18); the action of ACh is determined by the G_i protein subunits. Via a direct pathway, a G_i protein βγ-subunit activates inwardly rectifying muscarinic K^+ (K_{ACh}) channels in the sinoatrial node cells (11, 28, 35); K_{ACh} channels then exert a negative chronotropic effect by hyperpolarizing the sinoatrial node cells. On the other hand, via an indirect pathway, a G_i protein α-subunit suppresses adenylyl cyclase (12, 32); the suppression of adenylyl cyclase then decreases HR by inhibiting inward currents in the sinoatrial node cells, which are activated by cAMP or cAMP-dependent protein kinase. However, functional roles of the direct and indirect actions of ACh are not fully understood in the overall picture of vagal control of HR.

As a function in the dual control of adenylyl cyclase by G protein (12), the indirect action of ACh counteracts the G_s proteins activated by β_1-adrenergic sympathetic stimulation and relies on slower changes in intracellular cAMP levels (8). On the contrary, the direct action of ACh utilizes the faster membrane-delimited mechanisms involving K_{ACh} channels (3) and is believed to be independent of sympathetic control. Given the rapidity of vagal HR control compared with sympathetic control (2, 14, 31), we hypothesized that the direct action of ACh via K_{ACh} channels contributes to the quickness of the vagal HR control in vivo. To test this hypothesis, we used the selective K_{ACh} channel blocker tertiapin to examine the dynamic and static transfer characteristics of the HR response to vagal stimulation (7, 10, 13, 15).

The pioneering work by Yamada (34) demonstrated that the direct action of ACh via K_{ACh} channels mediates ~75% of the steady-state negative chronotropic effects relative to the maximum carbachol-induced bradycardia in the isolated rabbit heart (i.e., static HR response to vagal stimulation). However, in this study, the role of K_{ACh} channels in the dynamic HR response to vagal stimulation was not analyzed quantitatively. Because HR changes dynamically in response to daily activities, quantification of dynamic and static characteristics is equally important. For instance, information on the dynamic HR response is key to understanding the generation of HR variability. Berger et al. (2) used transfer function analysis to identify the dynamic characteristics of the HR response. Saul et al. (29) demonstrated the utility of transfer function analysis for insight into cardiovascular regulation. The present study aims to expand our knowledge of the involvement of K_{ACh} channels in dynamic HR control by the vagal system.

MATERIALS AND METHODS

Surgical preparations. Animal care was consistent with the "Guiding Principles for Care and Use of Animals in the Field of Physiological Sciences," of the Physiological Society of Japan. All protocols were reviewed and approved by the Animal Subjects Committee of the National Cardiovascular Center. Nine Japanese White rabbits (2.5–3.2 kg body wt) were anesthetized by a mixture of urethane (250 mg/ml) and α-chloralose (40 mg/ml): initiation with a bolus injection of 2 ml/kg and maintenance with continuous administration at 0.5

Address for reprint requests and other correspondence: M. Mizuno, Dept. of Cardiovascular Dynamics, Advanced Medical Engineering Center, National Cardiovascular Center Research Institute, 5-7-1 Fujishirodai, Suita, Osaka 565-8565, Japan (e-mail: m-mizuno@ri.ncvc.go.jp).

The costs of publication of this article were defrayed in part by the payment of page charges. The article must therefore be hereby marked "*advertisement*" in accordance with 18 U.S.C. Section 1734 solely to indicate this fact.

$ml \cdot kg^{-1} \cdot h^{-1}$. The rabbits were intubated and mechanically ventilated with oxygen-enriched room air. Arterial pressure (AP) was measured by a micromanometer (model SPC-330A, Millar Instruments, Houston, TX) inserted into the right femoral artery and advanced to the thoracic aorta. HR was measured with a cardiotachometer (model N4778, San-ei, Tokyo, Japan). A double-lumen catheter was introduced into the right femoral vein for continuous anesthetic and drug administration. Sinoaortic denervation was performed bilaterally to minimize changes in the sympathetic efferent nerve activity via arterial baroreflexes. Bilateral section of the cardiac postganglionic sympathetic nerves minimized any possible interaction between the vagus and sympathetic nerves. The vagi were sectioned bilaterally at the neck. A pair of bipolar electrodes were attached to the cardiac end of the sectioned right vagus for vagal stimulation. Immersion of the stimulation electrodes and nerves in a mixture of white petroleum jelly (Vaseline) and liquid paraffin prevented drying and provided insulation. Body temperature was maintained at 38°C with a heating pad throughout the experiment.

Experimental procedures. The pulse duration of nerve stimulation was set at 2 ms. The stimulation amplitude of the right vagus was adjusted to yield an HR decrease of ~50 beats/min at a stimulation frequency of 10 Hz. After this adjustment, the amplitude of vagal stimulation was fixed at 1.8–6.0 V. Initiation of vagal nerve stimulation over 1 h upon completion of surgical preparations allowed stable hemodynamics. A preliminary examination indicated that the response of HR to vagal stimulation was stable for up to 3 h in our experimental settings (10 min of dynamic vagal stimulation at 50-min intervals; data not shown).

Dynamic protocol. For estimation of the dynamic transfer characteristics from vagal stimulation to HR response, the right vagus was stimulated by a frequency-modulated pulse train for 10 min. The stimulation frequency was switched every 500 ms at 0 or 10 Hz according to a binary white-noise signal. The power spectrum of the stimulation signal was reasonably constant up to 1 Hz. The transfer function was estimated up to 1 Hz, because the reliability of estimation decreased as a result of the diminution of input power above this frequency. The selected frequency range sufficiently spanned the physiological range of interest with respect to the dynamic vagal control of HR.

Static protocol. For estimation of the static transfer characteristics from vagal stimulation to HR response, step-wise vagal stimulation was performed. Vagal stimulation frequency was increased from 5 to 20 Hz in 5-Hz increments. Each frequency step was maintained for 60 s.

The dynamic and static transfer functions from vagal stimulation to HR response were estimated under control and K_{ACh} channel blockade conditions. After the control data were recorded, a bolus injection (30 nmol/kg iv) of a selective K_{ACh} channel blocker, tertiapin (Peptide Institute, Osaka, Japan), was administered, and vagal stimulation protocols were repeated 15 min thereafter. The control data were obtained first in all animals, because the long-lasting (>2 h) effects of tertiapin (data not shown) did not permit the subsequent acquisition of control data. A >5-min interval between dynamic and step-wise stimulation protocols confirmed that AP and HR returned to baseline levels. Dynamic and step-wise vagal stimulation protocols were randomly assigned under control and K_{ACh} channel blockade conditions.

β-Adrenergic blockade protocol. A supplemental experiment was performed under β-adrenergic blockade ($n = 3$) eliminated any effect of sympathetic activity. At ~10 min after a bolus injection of propranolol (1 mg/kg iv) (22), HR and AP reached a new steady state. The dynamic and static transfer functions from vagal stimulation to HR response were estimated before and after tertiapin treatment, both under β-adrenergic blockade.

Data analysis. A 12-bit analog-to-digital converter was used to digitize data at 200 Hz, and data were stored on the hard disk of a dedicated laboratory computer system. The dynamic transfer function from binary white-noise vagal stimulation to HR response was estimated as follows. Input-output data pairs of the vagal stimulation frequency and HR were resampled at 10 Hz; then data pairs were partitioned into eight 50%-overlapping segments consisting of 1,024 data points each. For each segment, the linear trend was subtracted, and a Hanning window was applied. A fast Fourier transform was then performed to obtain the frequency spectra for vagal stimulation [$N(f)$] and HR [$HR(f)$] (4). Over the eight segments, the power of vagal stimulation [$S_{N \cdot N}(f)$], the power of HR [$S_{HR \cdot HR}(f)$], and the cross power between these two signals [$S_{N \cdot HR}(f)$] were ensemble averaged. Finally, the transfer function [$H(f)$] from vagal stimulation to the HR response was determined as follows (1, 20)

$$H(f) = \frac{S_{N \cdot HR}(f)}{S_{N \cdot N}(f)} \tag{1}$$

The transfer function from vagal stimulation to HR response approximated a first-order, low-pass filter with a lag time in previous studies (14, 21–24); therefore, the estimated transfer function was parameterized as follows

$$H(f) = \frac{-K}{1 + \frac{f}{f_C} j} e^{-2\pi f j L} \tag{2}$$

where K represents the dynamic gain (or, more precisely, the steady-state gain, in $beats \cdot min^{-1} \cdot Hz^{-1}$), f_c denotes the corner frequency (in Hz), L denotes the lag time (in s), and f and j represent frequency and the imaginary unit, respectively. The negative sign in the numerator indicates the negative HR response to vagal stimulation. The steady-state gain indicates the asymptotic value of the relative amplitude of the HR response to vagal nerve stimulation obtained in the frequency of input modulation approaching zero. The corner frequency represents the frequency of input modulation at which gain decreases by 3 dB from the steady-state gain in the frequency domain and reflects the readiness of the HR response for vagal stimulation in the time domain. The dynamic gain, corner frequency, and lag time were estimated by an iterative nonlinear least-squares regression. The phase shift of the transfer function indicates, with respect to the input signal, a lag or lead in the output signal normalized by its corresponding frequency of input modulation.

To quantify the linear dependence of the HR response on vagal stimulation, the magnitude-squared coherence function [$Coh(f)$] was estimated as follows (1, 20)

$$Coh(f) = \frac{|S_{N \cdot HR}(f)|^2}{S_{N \cdot N}(f) \cdot S_{HR \cdot HR}(f)} \tag{3}$$

Coherence values range from zero to unity. Unity coherence indicates perfect linear dependence between the input and output signals; in contrast, zero coherence indicates total independence between the two signals.

To facilitate the intuitive understanding of the system dynamic characteristics, we calculated the system step response of HR to 1-Hz nerve stimulation as follows. The system impulse response was derived from the inverse Fourier transform of $H(f)$. The system step response was then obtained from the time integral of the impulse response. The length of the step response was 51.2 s. We calculated the maximum step response by averaging the last 10 s of the step response. The 90% rise time of the step response was determined as the time required for the response to reach 90% of the maximum step response. The time constant of the step response was calculated from the corner frequency of the corresponding transfer function as follows

$$\text{time constant} = \frac{1}{2 \cdot \pi \cdot fc} \tag{4}$$

where the time constant is related inversely to the corner frequency without influence of the lag time.

The static transfer function from step-wise vagal stimulation to HR was estimated by averaging the HR data during the final 10 s of the 60-s stimulation at each stimulation frequency.

Statistical analysis. Values are means ± SD. Student's paired *t*-test was used to test differences in fitted parameters and calculated step response between control and K_{ACh} channel blockade conditions. For hemodynamic parameters, a two-way ANOVA, with drug and vagal stimulation as the main effects, was used to determine significant differences. For percent reduction from the control conditions in each parameter, one-way ANOVA was used to determine significant differences. $P < 0.05$ was considered significant.

RESULTS

Dynamic characteristics. Figure 1*A* shows typical recordings and corresponding power spectra of vagal stimulation and HR response under control and K_{ACh} channel blockade conditions. Random vagal stimulation decreased HR intermittently. Tertiapin-mediated K_{ACh} channel blockade attenuated the amplitude of the variation and the speed of the HR response to vagal stimulation. In the power spectral plot, tertiapin decreased the HR power. The decrease in the HR power was

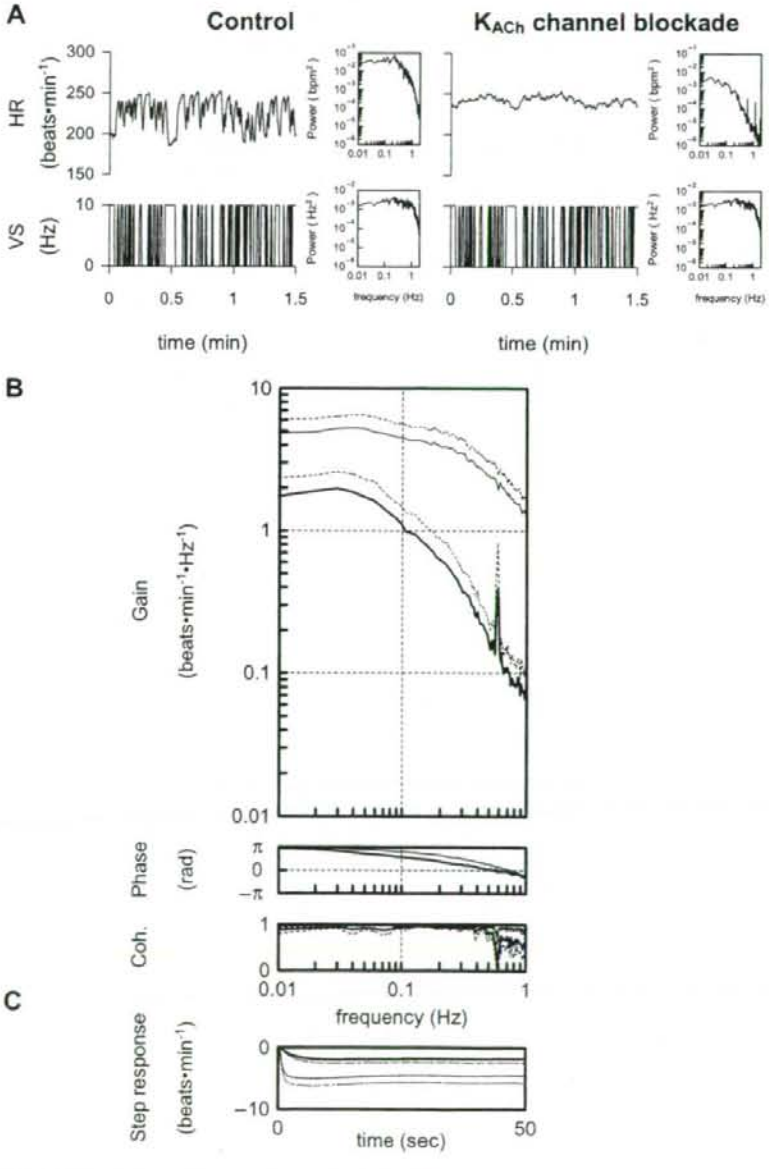

Fig. 1. *A*: representative recordings of heart rate (HR) obtained utilizing binary white-noise vagal stimulation (*top*) and corresponding vagal stimulation (VS, *bottom*). Traces were recorded before (control, *left*) and after tertiapin infusion (30 nmol/kg iv) for muscarinic K^+ (K_{ACh}) channel blockade (*right*). *Insets*: power spectra of each parameter. Tertiapin attenuated amplitude of HR variation and speed of response of HR to vagal stimulation. *B*: dynamic transfer function relating vagal stimulation to HR responses averaged from all animals (pooled data, $n = 9$). *Top*: gains; *middle*: phase shifts; *bottom*: coherence (Coh) functions. Frequency on abscissa (gain and phase) indicates frequency of input modulation, rather than stimulation frequency. *C*: calculated step response to 1-Hz tonic vagal stimulation averaged from all animals (pooled data, $n = 9$). Solid lines, means; dashed lines, SD. Thin line, control; thick line, K_{ACh} channel blockade with tertiapin (30 nmol/kg iv). Tertiapin decreased transfer gain and increased phase shift with increasing frequency, and tertiapin decreased maximum step response and slowed initial step response.

Table 1. *Effects of tertiapin infusion on AP and HR before and during dynamic vagal stimulation*

	Control	Tertiapin
AP, mmHg		
Before stimulation	82.4±20.5	77.6±20.7
During stimulation	77.9±20.0	74.8±18.6
HR, beats/min		
Before stimulation	247.3±24.7	248.1±32.7
During stimulation	212.4±22.3	231.1±25.9

Values are means ± SD ($n = 9$). Tertiapin was infused at 30 nmol/kg iv. AP, arterial pressure; HR, heart rate. Vagal stimulation significantly decreased HR ($P < 0.01$), but no significant effect of drug ($P = 0.28$) or interaction ($P = 0.32$) was observed by 2-way ANOVA.

more potent in the higher (>0.1 Hz) than in the lower frequency range.

Table 1 summarizes the mean values of AP and HR before and during vagal stimulation averaged from all animals. Dynamic vagal stimulation significantly decreased the mean HR ($P < 0.01$), but not the mean AP. Tertiapin did not significantly affect mean AP or HR before or during stimulation.

Figure 1*B* illustrates the dynamic transfer functions characterizing the vagal HR response averaged from all animals under control and tertiapin-mediated K_{ACh} channel blockade conditions. Gain plots, phase plots, and coherence functions are shown. Tertiapin attenuated the dynamic gain compared with the control conditions; the extent of the attenuation was greater in the higher frequency range: 63.0 ± 11.6, 74.4 ± 8.3, 93.0 ± 2.5, and 93.3 ± 3.9% at 0.01. 0.1, 0.5, and 1 Hz, respectively, as normalized to the control condition ($P < 0.01$ by ANOVA). The peak in the gain at 0.6 Hz observed during tertiapin-mediated K_{ATP} channel blockade would be caused by the artificial respiration (respiratory rate = 35–40 min^{-1}), because the low coherence value (~0.1) at 0.6 Hz indicates the independence of the input and output signals. This peak was masked by the large HR response to vagal stimulation under the control condition. The phase approached π radians at the lowest frequency and lagged with increasing frequency under the control condition; tertiapin caused the phase difference between the two conditions in the frequency range of 0.03–0.7 Hz, which disappeared at 1 Hz. The fitted parameters of the transfer functions are summarized in Table 2. Tertiapin significantly decreased the dynamic gain and the corner frequency without changing the lag time. Coherence was near unity in the overall frequency range in the control condition, whereas a decrease in the coherence function from unity was noted at >0.6 Hz with K_{ACh} channel blockade.

Figure 1*C* shows the calculated step response of HR to vagal stimulation averaged from all animals in the control condition and during K_{ACh} channel blockade. Tertiapin slowed the transient response (time constants = 0.6 ± 0.1 to 2.7 ± 0.5 s, $P < 0.01$) and attenuated the HR response to vagal stimulation (maximum step response = −4.5 ± 1.2 to −1.8 ± 0.6 beats/min, $P < 0.01$) in the time domain. Furthermore, tertiapin significantly delayed the 90% rise time of the step response, which was calculated as an index of system readiness (1.6 ± 0.5 to 5.0 ± 1.4 s, $P < 0.01$).

Static characteristics. Figure 2*A* shows typical recordings of step-wise vagal stimulation and the HR response in the control condition and during K_{ACh} channel blockade. The step-wise vagal stimulation decreased HR in a step-wise manner. Tertiapin attenuated the static reductions of HR from the baseline HR.

Figure 2*B* summarizes changes in HR in response to step-wise vagal stimulation. The step-wise vagal stimulation significantly decreased HR with increasing stimulus frequency under both conditions. Tertiapin significantly attenuated the static reductions of HR. The attenuation of HR reduction normalized to control conditions increased with increasing stimulus frequency: 45.8 ± 21.3, 58.2 ± 17.9, 64.7 ± 14.6, and 68.0 ± 11.4% at 5, 10, 15, and 20 Hz, respectively ($P < 0.05$ by ANOVA).

β-Adrenergic blockade protocol. In the supplemental protocol ($n = 3$) with β-adrenergic blockade, tertiapin decreased the dynamic gain from 2.4 ± 0.6 to 1.3 ± 0.5 beats·min^{-1}·Hz^{-1} and the corner frequency from 0.23 ± 0.05 to 0.06 ± 0.02 Hz without changing the lag time (0.36 ± 0.01 vs. 0.43 ± 0.00 s). In terms of the static characteristics, tertiapin significantly attenuated the vagal stimulation-induced HR decrease by 43 ± 10, 50 ± 8, 56 ± 7, and 61 ± 8% at stimulus frequencies of 5, 10, 15, and 20 Hz, respectively.

DISCUSSION

We have quantified the role of the K_{ACh} channels by examining the transfer characteristics. The major findings in the present study are that K_{ACh} channel blockade with intravenous tertiapin administration decreased the dynamic gain and corner frequency without changing the lag time of the dynamic transfer function from vagal stimulation to HR. These findings support our hypothesis that direct action of ACh via K_{ACh} channels contributes to the quickness of the HR control in response to electrical vagal stimulation.

Effect of tertiapin on dynamic transfer characteristics. Our results indicate that K_{ACh} channels contribute to a rapid component in vagal HR control. Tertiapin slowed the dynamic HR response to vagal stimulation, since tertiapin attenuated the gain of the transfer function significantly in the high frequency range (Fig. 1*B*). Moreover, the calculated step response clearly demonstrated this point (Fig. 1*C*). Tertiapin prolonged the time constant and 90% rise time of the step response by 2.1 and 3.4 s, respectively. Since quickness is a hallmark of the vagal control of HR relative to sympathetic control, these results highlight the importance of K_{ACh} channels in the rapidity of vagal HR control. Because tertiapin did not affect the lag time (Table 2), the increase in the 90% rise time to the step response due to tertiapin (−3.4 s) may primarily reflect the slowed transient response.

Our results are consistent with and may partly explain the earlier studies in which transgenic mice were used to investigate the role of K_{ACh} channels (8, 33). Using the G protein-

Table 2. *Effects of tertiapin infusion on parameters of the transfer function relating dynamic vagal stimulation to HR*

	Control	Tertiapin
Dynamic gain, beats·min^{-1}·Hz^{-1}	5.0±1.2	2.0±0.6*
Corner frequency, Hz	0.25±0.03	0.06±0.01*
Lag time, s	0.37±0.04	0.39±0.05

Values are means ± SD. Tertiapin was infused at 30 nmol/kg iv. *$P < 0.01$ vs. corresponding control.

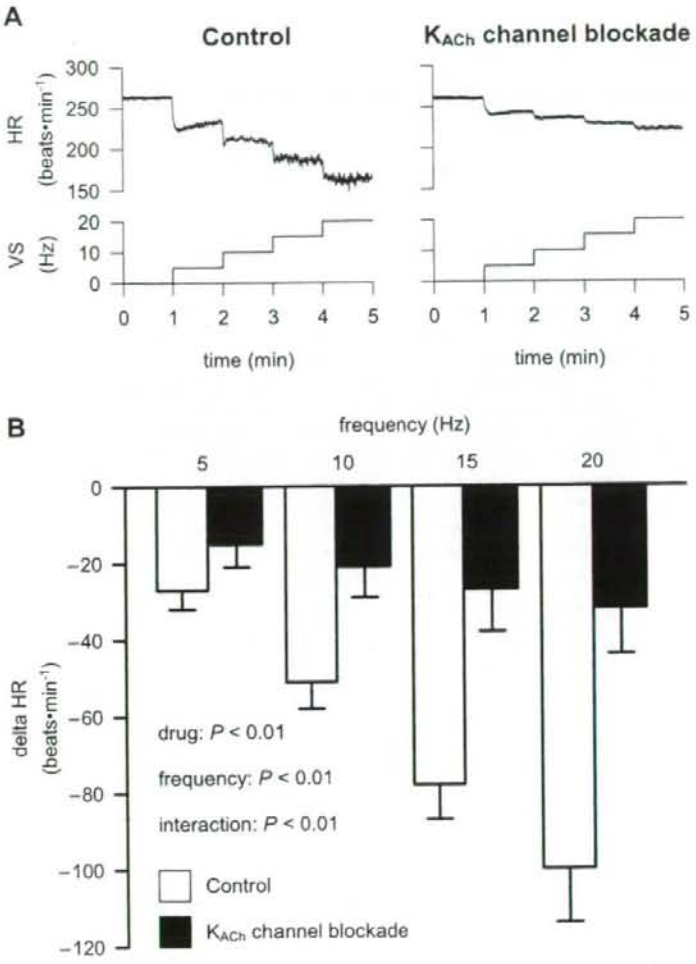

Fig. 2. *A*: representative recordings of HR (*top*) and corresponding vagal stimulation (*bottom*) obtained utilizing a step-wise stimulation. Traces were recorded before (control, *left*) and after tertiapin infusion (30 nmol/kg iv) for K_{ACh} channel blockade (*right*). K_{ACh} channel blockade attenuated amplitude of HR variation to tonic vagal stimulation. *B*: static transfer function relating step-wise vagal stimulation to HR responses averaged from all animals (pooled data, $n = 9$). Basal HR was not different between control and K_{ACh} channel blockade (see Table 1). K_{ACh} channel blockade decreases static HR response, and static reductions in bradycardic effect were greater at higher stimulation frequencies.

gated inwardly rectifying potassium (GIRK) channel family subunit GIRK4, which is a component of K_{ACh} channels (5, 16), Wickman et al. (33) indicated that the spectral power of HR was lower at 1.5–5.0 Hz, which is predominantly vagally mediated, but not at <0.4 Hz, in GIRK4-knockout than in wild-type mice. Another study using transgenic mice with a reduction in functional βγ-subunits of the G_i proteins also showed impaired vagal HR control, such as reductions in carbachol-induced bradycardia, HR variability, and baroreflex sensitivity (8). In the present study, tertiapin significantly attenuated the dynamic gain compared with the control conditions in the frequency bands from 0.01 to 1 Hz; the extent of the decreases in dynamic gain was augmented with increasing frequency of input modulation. This finding also supports the notion that K_{ACh} channels play a large part as a rapid component of vagal control of HR. Furthermore, increased phase shift due to tertiapin in the higher frequency range (0.03–0.7 Hz) would support the interpretation that the K_{ACh} channel current played an important role in the rapid HR response to vagal stimulation.

Tertiapin-mediated changes in fitted parameters of the transfer function from vagal stimulation to HR suggest that, at the postjunctional effector sites, the K_{ACh} channels play a key role in determining the dynamic properties of transduction from vagal nerve activity to HR. To quantitatively elucidate vagal and sympathetic control of HR, our research group used a transfer function analysis to examine the system characteristics. First, the transfer function from dynamic vagal nerve stimulation to HR approximated the characteristics of a first-order, low-pass filter, whereas the transfer function from dynamic sympathetic nerve stimulation to HR approximated the characteristics of a second-order, low-pass filter (14). Dynamic gain of vagal stimulation to HR was increased by concomitant sympathetic nerve stimulation (14) and pharmacologically induced accumulation of cAMP at the postjunctional effector sites (23) and decreased by high plasma norepinephrine (21). These perturbations of the indirect action of ACh did not affect the quickness of vagal HR control; i.e., neither corner frequency nor lag time was altered. On the contrary, inhibition of cholinesterase by neostigmine decreased the corner frequency

and increased the lag time (24). Taken together, these results might suggest that not only ACh kinetics at the neuroeffector site, but also the K_{ACh} channels at the postjunctional effector sites, play a key role in determining the dynamic properties of transduction from vagal nerve activity to HR.

Effect of tertiapin on the static transfer characteristics. Tertiapin attenuates the static reduction of HR in accord with the attenuation of the gain of the dynamic transfer function at the lowest frequency of input modulation. This suggests that K_{ACh} channels contribute to the static, as well as the rapid, component of vagal HR control. The relative attenuation of HR reduction increased with increasing stimulus frequency (Fig. 2*B*), suggesting that direct action of ACh in the static properties of transduction from vagus nerve activity to HR is augmented by an increase in the amount of available ACh. Although it is well established that the muscarinic response to static vagal stimulation depends on the stimulation frequency (26, 27), whether the contribution of the K_{ACh} channel pathway to the total HR response depends on the stimulus frequency remains unknown. The basal mean HR of GIRK-knockout mice (33) and transgenic mice with a reduction of βγ-subunits of the G_i proteins (8) is the same as that of wild-type mice, suggesting that K_{ACh} channels are not involved in mean HR control in the basal state. At low-to-moderate levels of vagal activity, vagal control of HR is due to changes in cAMP-modulated I_h, often referred to as "pacemaker" current (6). K_{ACh} channels might play an essential role in HR control at high levels of vagal activity.

In the present study, tertiapin decreased the HR response to vagal stimulation by ~70% of the control condition at a stimulus intensity of 20 Hz. This value is consistent with the earlier study by Yamada (34). This consistency suggested that K_{ACh} channels contribute to ~70% of the maximum negative chronotropic effects to pharmacologically and/or electronically induced vagal stimulation. However, changes in HR induced by tertiapin may have in turn affected the indirect action of ACh in the present study. Therefore, the percentage of direct vs. indirect action should be carefully interpreted.

Limitations. There are several limitations to this study. First, we did not confirm the completeness of K_{ACh} channel blockade. Kitamura et al. (15) demonstrated that tertiapin potently and selectively blocked the K_{ACh} channel in cardiac myocytes in a muscarinic receptor- and voltage-independent manner. Furthermore, Drici et al. (7) showed that tertiapin blocked K_{ACh} channels with an IC_{50} of ~30 nM with no significant effect on major currents associated with the cardiac repolarization process or atrioventricular conduction. On the basis of these studies, Hashimoto et al. (10) demonstrated that tertiapin (12 nmol/kg iv) significantly prolonged the atrial effective refractory period during vagal stimulation in their in vivo canine study. Therefore, we believe that the dose of tertiapin (30 nmol/kg iv) used in the present study should be sufficient to block K_{ACh} channel current in vivo.

Second, data were obtained from anesthetized animals. Since the anesthesia would affect the autonomic tone, the results may not be directly applicable to conscious animals. However, because we cut and stimulated the right cardiac vagal nerve, changes in autonomic outflow associated with anesthesia might not have significantly affected the results.

Third, in the present study, we stimulated the vagal nerve according to binary white noise and a step-wise pattern, which was quite different from the pattern of physiological neuronal discharge. However, although nonphysiological patterns of stimulation could theoretically bias the system identification results, because coherence was near unity over the frequency range of interest, by virtue of their inherent linearity, the system properties would not vary much with differing patterns of stimulation.

In conclusion, K_{ACh} channel blockade with intravenous tertiapin administration decreased the dynamic gain and corner frequency without changing the lag time of the transfer function from vagal stimulation to HR. In the time domain, tertiapin prolonged the time constant and 90% rise time of the step response. Additionally, tertiapin decreased the static reductions of HR from baseline HR to less than half of the control response with increasing vagal stimulus frequency. These results suggest that K_{ACh} channels accelerate the dynamic HR response to vagal stimulation and contribute more to the static HR response for more potent tonic vagal stimulation in vivo.

Perspectives

To simply identify the role of K_{ACh} channels in vagal HR control, a previous study (34) and the present study completely and/or partially excluded background sympathetic tone. However, in the physiological condition, sympathetic tone affects vagal control of HR and vice versa [e.g., accentuated antagonism (17)]. Pathophysiological conditions such as chronic heart failure (25), hypertension (19), and obesity (30) reveal increased basal sympathetic nerve activity compared with the normal condition. Tertiapin did not affect basal AP or HR (Table 1), suggesting that tertiapin did not affect sympathetic tone in the present experimental settings. Furthermore, under β-adrenergic blockade (the supplemental protocol), tertiapin decreased the dynamic gain and corner frequency, suggesting that the effects of tertiapin cannot be explained by the background sympathetic tone. However, the experimental design of the present study did not allow separate assessment of the direct vs. the indirect action of ACh, because the indirect action of ACh was not manipulated intentionally. Further investigation is needed to clarify the effects of sympathetic tone on the contribution of K_{ACh} channels to negative chronotropic effects.

GRANTS

This study was supported by Health and Labour Sciences Research Grants H15-Physi-001, H18-Nano-Ippan-003, and H18-Iryo-Ippan-023 from the Ministry of Health, Grant-in-Aid for Scientific Research promoted by the Ministry of Education, Culture, Sports, Science and Technology in Japan 18591992, and the Ground-Based Research Announcement for Space Utilization project promoted by the Japan Space Forum. This study was also supported by Industrial Technology Research Program Grant 06B44524a from the New Energy and Industrial Technology Development Organization of Japan.

REFERENCES

1. **Bendat J, Piersol A.** Single-input/output relationships. In: *Random Data Analysis and Measurement Procedures* (3rd ed). New York: Wiley, 2000, p. 189–217.
2. **Berger RD, Saul JP, Cohen RJ.** Transfer function analysis of autonomic regulation. I. Canine atrial rate response. *Am J Physiol Heart Circ Physiol* 256: H142–H152, 1989.
3. **Breitwieser GE, Szabo G.** Uncoupling of cardiac muscarinic and β-adrenergic receptors from ion channels by a guanine nucleotide analogue. *Nature* 317: 538–540, 1985.
4. **Brigham E.** FFT transform application. In: *The Fast Fourier Transform and Its Application.* Englewood Cliffs, NJ: Prentice-Hall, 1988, p. 167–203.

5. **Dascal N, Schreibmayer W, Lim NF, Wang W, Chavkin C, DiMagno L, Labarca C, Kieffer BL, Gaveriaux-Ruff C, Trollinger D, Lester HA, Davidson N.** Atrial G protein-activated K^+ channel: expression, cloning, and molecular properties. *Proc Natl Acad Sci USA* 90: 10235–10239, 1993.
6. **DiFrancesco D.** Cardiac pacemaker: 15 years of "new" interpretation. *Acta Cardiol* 50: 413–427, 1995.
7. **Drici MD, Diochot S, Terrenoire C, Romey G, Lazdunski M.** The bee venom peptide tertiapin underlines the role of $I_{K\,ACh}$ in acetylcholine-induced atrioventricular blocks. *Br J Pharmacol* 131: 569–577, 2000.
8. **Gehrmann J, Meister M, Maguire CT, Martins DC, Hammer PE, Neer EJ, Berul CI, Mende U.** Impaired parasympathetic heart rate control in mice with a reduction of functional G protein βγ-subunits. *Am J Physiol Heart Circ Physiol* 282: H445–H456, 2002.
9. **Hartzell HC, Mery PF, Fischmeister R, Szabo G.** Sympathetic regulation of cardiac calcium current is due exclusively to cAMP-dependent phosphorylation. *Nature* 351: 573–576, 1991.
10. **Hashimoto N, Yamashita T, Tsuruzoe N.** Tertiapin, a selective $I_{K\,ACh}$ blocker, terminates atrial fibrillation with selective atrial effective refractory period prolongation. *Pharmacol Res* 54: 136–141, 2006.
11. **Huang CL, Slesinger PA, Casey PJ, Jan YN, Jan LY.** Evidence that direct binding of Gβγ to the GIRK1 G protein-gated inwardly rectifying K^+ channel is important for channel activation. *Neuron* 15: 1133–1143, 1995.
12. **Irisawa H, Brown HF, Giles W.** Cardiac pacemaking in the sinoatrial node. *Physiol Rev* 73: 197–227, 1993.
13. **Jin W, Lu Z.** Synthesis of a stable form of tertiapin: a high-affinity inhibitor for inward-rectifier K^+ channels. *Biochemistry* 38: 14286–14293, 1999.
14. **Kawada T, Ikeda Y, Sugimachi M, Shishido T, Kawaguchi O, Yamazaki T, Alexander J Jr, Sunagawa K.** Bidirectional augmentation of heart rate regulation by autonomic nervous system in rabbits. *Am J Physiol Heart Circ Physiol* 271: H288–H295, 1996.
15. **Kitamura H, Yokoyama M, Akita H, Matsushita K, Kurachi Y, Yamada M.** Tertiapin potently and selectively blocks muscarinic K^+ channels in rabbit cardiac myocytes. *J Pharmacol Exp Ther* 293: 196–205, 2000.
16. **Krapivinsky G, Gordon EA, Wickman K, Velimirovic B, Krapivinsky L, Clapham DE.** The G-protein-gated atrial K^+ channel $I_{K\,ACh}$ is a heteromultimer of two inwardly rectifying K^+-channel proteins. *Nature* 374: 135–141, 1995.
17. **Levy MN.** Sympathetic-parasympathetic interactions in the heart. *Circ Res* 29: 437–445, 1971.
18. **Luetje CW, Tietje KM, Christian JL, Nathanson NM.** Differential tissue expression and developmental regulation of guanine nucleotide binding regulatory proteins and their messenger RNAs in rat heart. *J Biol Chem* 263: 13357–13365, 1988.
19. **Mancia G, Grassi G, Giannattasio C, Seravalle G.** Sympathetic activation in the pathogenesis of hypertension and progression of organ damage. *Hypertension* 34: 724–728, 1999.
20. **Marmarelis P, Marmarelis V.** The white noise method in system identification. In: *Analysis of Physiological Systems*. New York: Plenum, 1978, p. 131–221.
21. **Miyamoto T, Kawada T, Takaki H, Inagaki M, Yanagiya Y, Jin Y, Sugimachi M, Sunagawa K.** High plasma norepinephrine attenuates the dynamic heart rate response to vagal stimulation. *Am J Physiol Heart Circ Physiol* 284: H2412–H2418, 2003.
22. **Miyamoto T, Kawada T, Yanagiya Y, Inagaki M, Takaki H, Sugimachi M, Sunagawa K.** Cardiac sympathetic nerve stimulation does not attenuate dynamic vagal control of heart rate via α-adrenergic mechanism. *Am J Physiol Heart Circ Physiol* 287: H860–H865, 2004.
23. **Nakahara T, Kawada T, Sugimachi M, Miyano H, Sato T, Shishido T, Yoshimura R, Miyashita H, Inagaki M, Alexander J Jr, Sunagawa K.** Accumulation of cAMP augments dynamic vagal control of heart rate. *Am J Physiol Heart Circ Physiol* 275: H562–H567, 1998.
24. **Nakahara T, Kawada T, Sugimachi M, Miyano H, Sato T, Shishido T, Yoshimura R, Miyashita H, Sunagawa K.** Cholinesterase affects dynamic transduction properties from vagal stimulation to heart rate. *Am J Physiol Regul Integr Comp Physiol* 275: R541–R547, 1998.
25. **Negrao CE, Rondon MU, Tinucci T, Alves MJ, Roveda F, Braga AM, Reis SF, Nastari L, Barretto AC, Krieger EM, Middlekauff HR.** Abnormal neurovascular control during exercise is linked to heart failure severity. *Am J Physiol Heart Circ Physiol* 280: H1286–H1292, 2001.
26. **Parker P, Celler BG, Potter EK, McCloskey DI.** Vagal stimulation and cardiac slowing. *J Auton Nerv Syst* 11: 226–231, 1984.
27. **Priola DV, Cote I.** Differential sensitivity of the canine heart to acetylcholine and vagal stimulation. *Am J Physiol Heart Circ Physiol* 234: H460–H464, 1978.
28. **Sakmann B, Noma A, Trautwein W.** Acetylcholine activation of single muscarinic K^+ channels in isolated pacemaker cells of the mammalian heart. *Nature* 303: 250–253, 1983.
29. **Saul JP, Berger RD, Albrecht P, Stein SP, Chen MH, Cohen RJ.** Transfer function analysis of the circulation: unique insights into cardiovascular regulation. *Am J Physiol Heart Circ Physiol* 261: H1231–H1245, 1991.
30. **Seals DR, Bell C.** Chronic sympathetic activation: consequence and cause of age-associated obesity? *Diabetes* 53: 276–284, 2004.
31. **Spear JF, Moore EN.** Influence of brief vagal and stellate nerve stimulation on pacemaker activity and conduction within the atrioventricular conduction system of the dog. *Circ Res* 32: 27–41, 1973.
32. **Sunahara RK, Dessauer CW, Gilman AG.** Complexity and diversity of mammalian adenylyl cyclases. *Annu Rev Pharmacol Toxicol* 36: 461–480, 1996.
33. **Wickman K, Nemec J, Gendler SJ, Clapham DE.** Abnormal heart rate regulation in GIRK4 knockout mice. *Neuron* 20: 103–114, 1998.
34. **Yamada M.** The role of muscarinic K^+ channels in the negative chronotropic effect of a muscarinic agonist. *J Pharmacol Exp Ther* 300: 681–687, 2002.
35. **Yamada M, Inanobe A, Kurachi Y.** G protein regulation of potassium ion channels. *Pharmacol Rev* 50: 723–760, 1998.

Gab family proteins are essential for postnatal maintenance of cardiac function via neuregulin-1/ErbB signaling

Yoshikazu Nakaoka,[1] Keigo Nishida,[2] Masahiro Narimatsu,[3] Atsunori Kamiya,[4] Takashi Minami,[5] Hirofumi Sawa,[6] Katsuya Okawa,[7] Yasushi Fujio,[8] Tatsuya Koyama,[1] Makiko Maeda,[8] Manami Sone,[1] Satoru Yamasaki,[2] Yuji Arai,[9] Gou Young Koh,[10] Tatsuhiko Kodama,[5] Hisao Hirota,[11] Kinya Otsu,[11] Toshio Hirano,[2,3] and Naoki Mochizuki[1]

[1]Department of Structural Analysis, National Cardiovascular Center Research Institute, Osaka, Japan. [2]Laboratory for Cytokine Signaling, RIKEN Research Center for Allergy and Immunology (RCAI), Yokohama, Japan. [3]Laboratory of Developmental Immunology, Osaka University Graduate School of Frontier Biosciences and Graduate School of Medicine, Osaka, Japan. [4]Department of Cardiovascular Dynamics, National Cardiovascular Center Research Institute, Osaka, Japan. [5]Laboratory for System Biology and Medicine, Research Center for Advanced Science and Technology, University of Tokyo, Tokyo, Japan. [6]Department of Molecular Pathobiology, Hokkaido University Research Center for Zoonosis Control, Sapporo, Japan. [7]Horizontal Medical Research Organization, Kyoto University Graduate School of Medicine, Kyoto, Japan. [8]Department of Clinical Evaluation of Medicines and Therapeutics, Osaka University Graduate School of Pharmaceutical Sciences, Osaka, Japan. [9]Department of Bioscience, National Cardiovascular Center Research Institute, Osaka, Japan. [10]Biomedical Research Center and Department of Biological Sciences, Korea Advanced Institute of Science and Technology, Daejeon, Republic of Korea. [11]Department of Cardiovascular Medicine, Osaka University Graduate School of Medicine, Osaka, Japan.

Grb2-associated binder (Gab) family of scaffolding adaptor proteins coordinate signaling cascades downstream of growth factor and cytokine receptors. In the heart, among EGF family members, neuregulin-1β (NRG-1β, a paracrine factor produced from endothelium) induced remarkable tyrosine phosphorylation of Gab1 and Gab2 via erythroblastic leukemia viral oncogene (ErbB) receptors. We examined the role of Gab family proteins in NRG-1β/ErbB-mediated signal in the heart by creating cardiomyocyte-specific Gab1/Gab2 double knockout mice (DKO mice). Although DKO mice were viable, they exhibited marked ventricular dilatation and reduced contractility with aging. DKO mice showed high mortality after birth because of heart failure. In addition, we noticed remarkable endocardial fibroelastosis and increase of abnormally dilated vessels in the ventricles of DKO mice. NRG-1β induced activation of both ERK and AKT in the hearts of control mice but not in those of DKO mice. Using DNA microarray analysis, we found that stimulation with NRG-1β upregulated expression of an endothelium-stabilizing factor, angiopoietin 1, in the hearts of control mice but not in those of DKO mice, which accounted for the pathological abnormalities in the DKO hearts. Taken together, our observations indicated that in the NRG-1β/ErbB signaling, Gab1 and Gab2 of the myocardium are essential for both maintenance of myocardial function and stabilization of cardiac capillary and endocardial endothelium in the postnatal heart.

Introduction

Dilated cardiomyopathy (DCM) is an common cause of heart failure. Epidemiological studies suggest that 25%–30% of DCM is inherited. Among the mutations associated with DCM in humans and mice, several involve genes encoding cytoskeletal proteins and sarcomere-related proteins (1); however, mutations in these known genes account for only a minor proportion of the heritable cardiomyopathies in humans. Cardiac function is maintained by cytokine- and growth factor–triggered intracellular signaling. Genetically modified mice, in which intracellular signaling molecules are either activated or perturbed, also exhibit cardiac dysfunction, suggesting that coordination of signal transduction systems is critical for the preservation of cardiac function (2).

The Grb2-associated binder (Gab) family proteins, which serve as scaffolding adaptor proteins, crucially intervene between receptors and intracellular signaling molecules to coordinate the signaling cascades of cytokines, growth factors, antigens, and numerous other molecules (3–5). Multiple phosphorylated tyrosine residues of Gab proteins become docking sites for Src homology-2 domain-containing molecules. Docking of Gab to tyrosine phosphatase SHP2 and the p85 regulatory subunit of PI3K leads to the activation of ERK and AKT, respectively (4, 5). Three Gab family members, Gab1, Gab2, and Gab3, have been identified in mammals and are structurally similar (4, 5). Conventional Gab1 knockout (Gab1KO) mice display embryonic lethality with impaired development of heart, placenta, skin, and muscle (6, 7). Gab2KO mice do not show any obvious developmental defects but display impaired allergic responses and osteoclast defects (8–11). Gab3KO mice exhibit no obvious phenotype (12).

We previously demonstrated the importance of Gab1-ERK5 signaling in cardiomyocyte hypertrophy through the leukemia inhibitory factor–gp130–dependent (LIF-gp130–dependent)

Nonstandard abbreviations used: Ang1, angiopoietin 1; ANP, atrial natriuretic peptide; DCM, dilated cardiomyopathy; DKO, cardiomyocyte-specific Gab1/Gab2 double knockout; EFE, endocardial fibroelastosis; EphA4, Eph receptor A4; ErbB, erythroblastic leukemia viral oncogene; Gab, Grb2-associated binder; Gab1CKO, cardiomyocyte-specific Gab1 conditional knockout; Gab1KO, conventional Gab1 knockout; HB-EGF, heparin-binding EGF-like growth factor; LIF, leukemia inhibitory factor; α-MHC, α-myosin heavy chain; NRG-1, neuregulin-1; α-SKA, skeletal α-actin; TSP1, thrombospondin 1.

Conflict of interest: The authors have declared that no conflict of interest exists.

Citation for this article: *J. Clin. Invest.* 117:1771–1781 (2007). doi:10.1172/JCI30651.

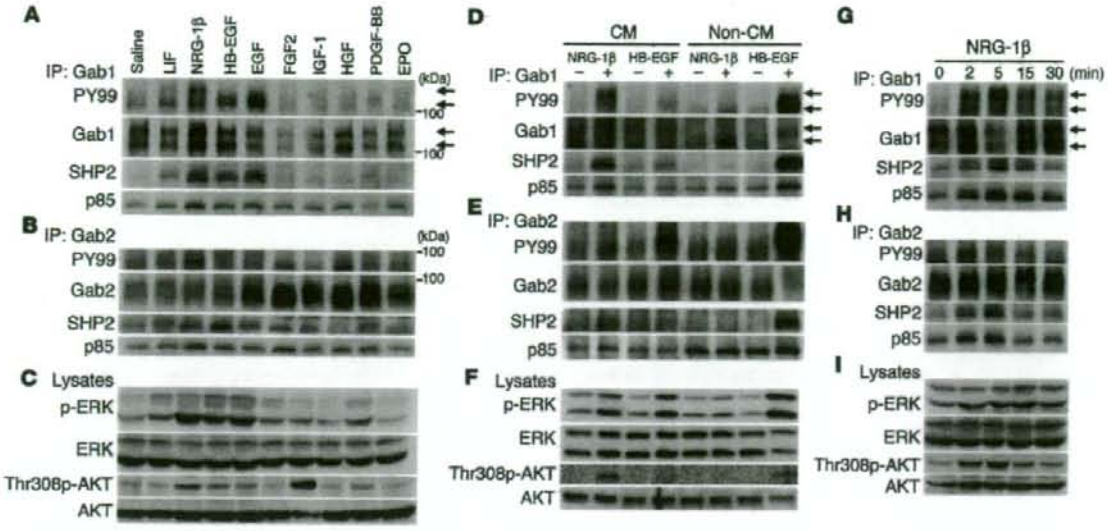

Figure 1

Gab1 and Gab2 are engaged in coordination of NRG-1β/ErbB signaling pathway in the myocardium. Tyrosine phosphorylation of Gab1 (**A**) and Gab2 (**B**) and their association with SHP2 and p85 were analyzed by IP of the heart lysates. Mouse heart lysates were prepared at 5 minutes after injection with the cytokines and growth factors listed at top. Heart lysates were subjected to IP with anti-Gab1 (**A**) or anti-Gab2 (**B**) serum, followed by IB analysis using the Ab indicated at the left. (**C**) Activation levels of ERK and AKT were assessed by phospho-specific Ab. Tyrosine phosphorylation of Gab1 (**D**) Gab2 (**E**) and their association with SHP2 and p85 was examined by IP of cell lysates from neonatal rat cardiomyocytes (CM) or noncardiomyocytes (non-CM) stimulated with either NRG-1β (50 ng/ml) or HB-EGF (50 ng/ml) for 5 minutes. IP complexes were subjected to IB using the Ab indicated at the left. (**F**) NRG-1β– and HB-EGF–dependent activation of ERK and AKT was examined in CM and non-CM as in **C**. Tyrosine phosphorylation of Gab1 (**G**) and Gab2 (**H**) and their association with SHP2 and p85 in the mouse hearts were analyzed after injection with 5 μg of NRG-1β as in **A** and **B**, respectively. Heart lysates were prepared at the indicated time after injection. Gab1 and Gab2 underwent tyrosine phosphorylation and associated with SHP2 and p85 in a time-dependent manner upon NRG-1β stimulation. (**I**) Activation of ERK and AKT were assessed as in **C**. Arrows denote 2 isoforms of Gab1. Representative blots of 3 experiments are shown. PY99, antibody recognizing phospho-tyrosine.

signaling pathway (13). Gab family proteins are also involved in EGF family–erythroblastic leukemia viral oncogene (EGF family–ErbB) receptor family signaling (6, 14, 15). EGF family–ErbB receptor signaling plays crucial roles in heart development and preservation of adult cardiac function (16, 17). Among the EGF family members, neuregulin-1 (NRG-1) (18) and heparin-binding EGF-like growth factor (HB-EGF) (19) are particularly important agonists for ErbB receptors on cardiomyocytes. NRG-1 serves as a paracrine factor that is shed from the endothelium and activates the ErbB4 homodimer or ErbB2/ErbB4 (also known as HER2/HER4) heterodimer on cardiomyocytes (16, 17, 20, 21). NRG-1–, ErbB2–, and ErbB4-deficient mice display embryonic lethality and similar defects in ventricular trabeculation (22–24). HB-EGF–deficient mice also display abnormal valvular development and cardiac dysfunction (25, 26).

The importance of ErbB signaling in the adult heart was first revealed by the unforeseen adverse effects of trastuzumab (Herceptin), a monoclonal Ab against ErbB2 used in the treatment of breast cancer. Trastuzumab induces heart failure when combined with anthracycline treatment (17, 27, 28). In addition to this clinical evidence, cardiomyocyte-specific ErbB2- and ErbB4-deficient mice both exhibit DCM (29–31). However, the precise intracellular signaling responsible for ErbB-regulated cardiac function is still unclear.

In the present study, we used myocardium-specific deletion of Gab family proteins in the mice to demonstrate that Gab1 and Gab2 in the myocardium are essential for transmitting the signal from NRG-1β/ErbB to directly maintain myocardial function and to subsequently stabilize capillary and endocardial endothelium in the postnatal heart.

Results

Gab1 and Gab2 are engaged in coordination of NRG-1β/ErbB signaling pathway in the myocardium. We aimed at exploring the function of Gab family proteins in the heart. Thus, we first examined the expression of Gab family transcripts by RT-PCR and detected the mRNA of Gab1 and Gab2, but not that of Gab3, in the murine heart (Supplemental Figure 1; supplemental material available online with this article; doi:10.1172/JCI30651DS1). To elucidate how Gab1 and Gab2 are involved in the intracellular signaling in the heart, mice were injected with various cytokines and growth factors. Among these agonists, ErbB receptor-activating agonists, including NRG-1β, HB-EGF, and EGF, induced strong tyrosine phosphorylation of Gab1 and Gab2 and the subsequent association of Gab1 and Gab2 with SHP2 and p85 (Figure 1, A and B). We identified 2 Gab1 isoforms, high-molecular weight (high-MW) Gab1 (120–130 kDa) and low-MW Gab1 (100 kDa). Notably, the high-MW Gab1 underwent tyrosine phosphorylation

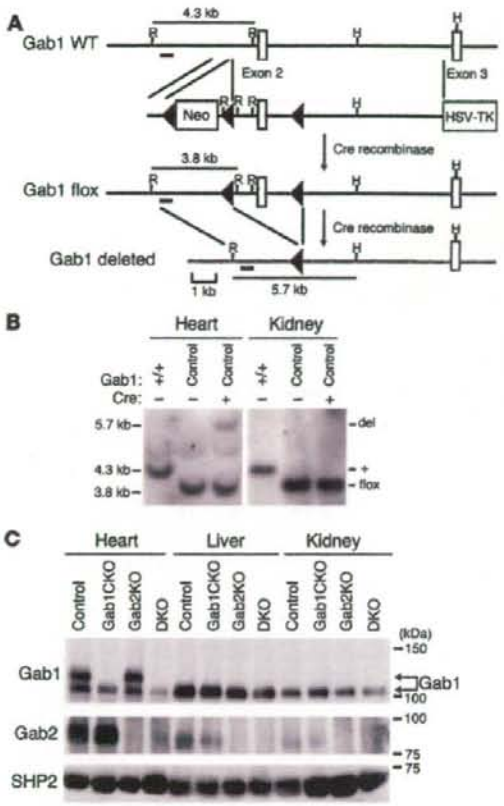

Figure 2

Generation of DKO mice. (**A**) Schematic illustration of genomic structure of the *Gab1* wild-type, *Gab1* flox, and *Gab1*-deleted alleles and a targeting vector. *loxP* sequences are indicated by black triangles. Restriction enzyme sites for *Eco*RI and *Hind*III are indicated as R and H, respectively. Fragments detected by the probe (short bold line) used for Southern blot analysis after digestion of genomic DNA with *Eco*RI and *Hind*III are indicated as solid lines measuring 4.3 kb, 3.8 kb, and 5.7 kb. HSV-TK, herpes simplex virus–thymidine kinase. (**B**) Southern blot analysis demonstrated recombination of the *Gab1*^{flox} allele in the heart, but not in the kidney, of *Gab1*$^{flox/flox}$ mice, which possessed the *α-MHC–Cre* allele. (**C**) Following IP, expression of Gab1 and Gab2 was examined by IB using anti-Gab1 (top row) and anti-Gab2 (middle row) serums. SHP2 was examined as a loading control (bottom row). Note that 2 isoforms of Gab1 were detected at the different MW exclusively in the heart (arrows) and that the high-MW Gab1 isoform in the heart was completely depleted in Gab1CKO and DKO. The low-MW Gab1 was also reduced by 80% in the heart of Gab1CKO and DKO mice compared with control and Gab2KO mice.

upon stimulation exclusively with NRG-1β, while low-MW Gab1 was phosphorylated by NRG-1β, HB-EGF, and EGF (Figure 1A). We confirmed that the high-MW Gab1 is a cardiac-specific isoform using molecular mass spectrometric analysis, which showed that the high-MW band that was recognized by anti-Gab1 Ab in Western blot analysis indeed contained the partial amino acid sequence of Gab1 (Supplemental Figure 2, A–C). Activation of both ERK and AKT was found only when stimulated with NRG-1β, HB-EGF, and EGF (Figure 1C), although activation of AKT was most strongly induced by IGF-1.

We examined whether the difference in Gab1 phosphorylation was due to the diversity of the cell types. To distinguish the signaling processes in cardiomyocytes from those in noncardiomyocytes, including fibroblasts, endothelial cells, and vascular smooth muscle cells in the heart, we analyzed the action of NRG-1β and HB-EGF in neonatal rat cardiomyocytes and noncardiomyocytes that had been isolated using the Percoll gradient method (32). NRG-1β induced tyrosine phosphorylation of Gab1 and Gab2, the subsequent association of Gab1 and Gab2 with SHP2 and p85, and the activation of ERK and AKT in cardiomyocytes but not in noncardiomyocytes (Figure 1, D–F). In clear contrast, HB-EGF induced those changes more strongly in noncardiomyocytes than in cardiomyocytes (Figure 1, D–F). It should be noted that tyrosine phosphorylation of the high-MW Gab1 in cardiomyocytes was induced after stimulation with NRG-1β but not with HB-EGF (Figure 1D). These findings suggest that NRG-1β acts as a highly selective agonist for cardiomyocytes, in agreement with previous reports (33).

Therefore, we focused on the NRG-1β–dependent signaling pathway through Gab1 and Gab2 in the murine hearts. Gab1 and Gab2 underwent tyrosine phosphorylation and associated with SHP2 and p85 after injection with NRG-1β in a time-dependent manner (Figure 1, G and H). In addition, both ERK and AKT were also activated by NRG-1β in a time-dependent manner (Figure 1I). We also checked the activation of ErbB family receptors of murine hearts stimulated with NRG-1β. NRG-1β induced tyrosine-phosphorylation of ErbB2 and ErbB4 but not that of ErbB1 (EGFR) or ErbB3 in accordance with a previous report in which cardiomyocytes were used in vitro (Supplemental Figure 3, A–D) (21). Furthermore, Gab1 associated with ErbB4 in a phosphorylation-dependent manner after injection with NRG-1β (Supplemental Figure 3E). These data suggest the engagement of Gab family proteins in the coordination of NRG-1β/ErbB signaling pathway.

Generation of cardiomyocyte-specific Gab1 conditional knockout mice. To elucidate the function of Gab family proteins in myocardium, we first generated cardiomyocyte-specific *Gab1* conditional knockout (Gab1CKO) mice using the Cre-*loxP* system. Using homologous recombination in embryonic stem cells, we created a *Gab1*^{flox} allele by introducing 2 loxP sites into introns flanking exon 2, which encodes part of the pleckstrin homology domain

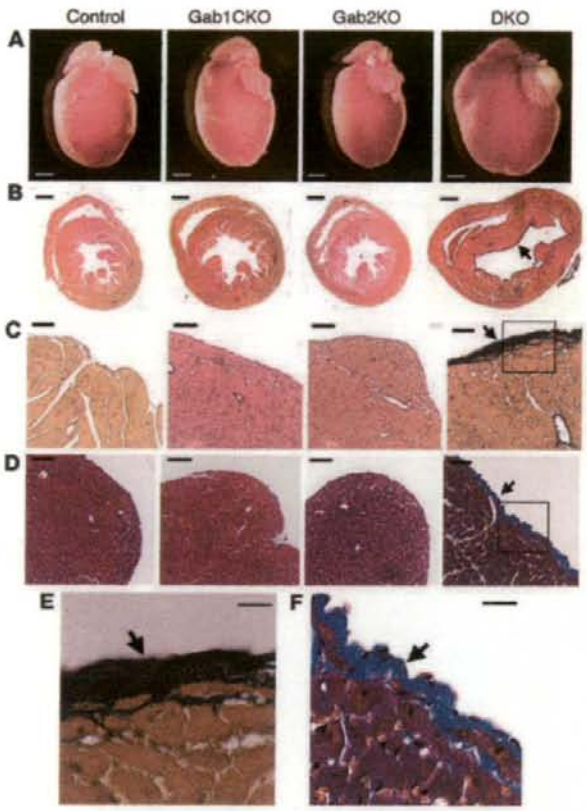

Figure 3
DKO mice display dilated cardiomyopathic features accompanied by EFE. (**A**) Representative images of whole hearts from 4 groups at 10 weeks of age. (**B**) Transverse sections of the hearts were stained using the elastica van Gieson method. DKO hearts showed marked biventricular dilation and slight wall thinning compared with the other 3 groups of hearts. (**C** and **E**) Higher magnification of elastica van Gieson–stained section of DKO heart shows the focal accumulation of elastic fibers (black) in the endocardium (arrows in **B** and **C**). (**D**) Masson's trichrome–stained section of DKO heart shows focal accumulation of collagen (blue) in the endocardium (arrow in **D**). (**E** and **F**) Boxed regions of **C** and **D**, respectively, are enlarged. Scale bars: 1 mm (**A** and **B**); 20 μm (**C**–**F**).

(Figure 2A). The protein expression of Gab1 in all tissues of mice homozygous for the Gab1-*loxP*–targeted allele (*Gab1*$^{flox/flox}$ mice) was almost the same level as in wild-type mice (data not shown). To cause recombination of the floxed allele exclusively in cardiomyocyte lineage, *Gab1*$^{flox/flox}$ mice were crossed with transgenic mice expressing *α-myosin heavy chain* promoter–driven Cre recombinase (*α-MHC–Cre* mice) (34, 35) (Figure 2A). We confirmed the Cre-mediated recombination during embryogenesis (E10.5 and E14.5) by crossing *α-MHC–Cre* mice with enhanced GFP reporter mice (Supplemental Figure 4A). The Gab1CKO (*Gab1*$^{flox/flox}$ *α-MHC-Cre(+)*) mice were born normally at the expected Mendelian frequency, whereas Gab1KO mice were embryonically lethal (6). In addition, the Gab1CKO mice displayed normal appearance and normal cardiac morphology at birth (Supplemental Figure 5A).

We observed the expected genetic recombination at the *Gab1* locus in the ventricles of Gab1CKO mouse hearts but not in other tissues (Figure 2B). In order to estimate the expression of Gab1 protein, immunoblot analyses were performed using the extracts from heart, liver, and kidney (Figure 2C). As described above, 2 isoforms of Gab1 proteins were detected in hearts, while low-MW Gab1 was commonly detected, suggesting that the high-MW Gab1 is a cardiac-specific isoform. Moreover, high-MW Gab1 protein was deleted in Gab1CKO hearts, suggesting that high-MW Gab1 is a product of the same *Gab1* gene that has low MW. In addition, we used Percoll gradient centrifugation to analyze the expression of Gab1 in cardiomyocytes and noncardiomyocytes isolated from neonatal rat hearts (32) and detected the high-MW isoform of Gab1 exclusively in cardiomyocytes (Supplemental Figure 2D).

In Gab1CKO mice, the high-MW Gab1 was completely deleted and the low-MW Gab1 was reduced to about 20% of control (*Gab1*$^{flox/flox}$) littermates. The residual low-MW Gab1 protein might be attributed to the noncardiomyocytes present in the heart. These data indicated the successful depletion of Gab1 in the cardiomyocytes (Figure 2C), because *α-MHC* promoter functions exclusively in the myocardium. In 3-day-old Gab1CKO mouse hearts, we detected an extent of Gab1 protein depletion similar to that of 3- or 10-week-old mice (Supplemental Figure 4B).

Generation of cardiomyocyte-specific Gab1/Gab2 double knockout mice. In murine hearts, mRNAs of Gab1 and Gab2 were detected by RT-PCR (Supplemental Figure 1). Gab2 can rescue the loss of Gab1 for activation of ERK in the EGF signaling pathway (36). We thus assumed that Gab2 might compensate for the deletion of Gab1 in the cardiomyocytes of Gab1CKO mice.

To completely deplete Gab family proteins in cardiomyocytes, Gab1CKO mice were crossed with Gab2KO mice. We created *Gab1*$^{flox/flox}$*Gab2*$^{-/-}$*α-MHC–Cre(+)* mice by crossing *Gab1*$^{+/flox}$*Gab2*$^{-/-}$*α-MHC–Cre(+)* mice with *Gab1*$^{flox/flox}$*Gab2*$^{-/-}$*α-MHC–Cre(−)* mice in the final breeding. The offspring of these crossings were recovered at expected Mendelian ratios as follows: *Gab1*$^{+/flox}$*Gab2*$^{-/-}$*α-MHC–Cre(−)* (n = 44; 24.6%); *Gab1*$^{+/flox}$*Gab2*$^{-/-}$*α-MHC–Cre(+)* (n = 46; 25.7%); *Gab1*$^{flox/flox}$*Gab2*$^{-/-}$*α-MHC–Cre(−)* (n = 39; 21.8%); *Gab1*$^{flox/flox}$*Gab2*$^{-/-}$*α-MHC–Cre(+)* (n = 50; 27.9%). Thereafter, we analyzed the following 4 groups of mice: *Gab1*$^{flox/flox}$*Gab2*$^{+/+}$*α-MHC–Cre(−)* (control); *Gab1*$^{flox/flox}$*Gab2*$^{+/+}$*α-MHC–Cre(+)* (Gab1CKO); *Gab1*$^{flox/flox}$*Gab2*$^{-/-}$*α-MHC–Cre(−)* (Gab2KO); and *Gab1*$^{flox/flox}$*Gab2*$^{-/-}$*α-MHC–Cre(+)* (DKO). Both Gab2KO and DKO mice displayed normal appearance and normal cardiac morphology at birth (Supplemental Figure 5A). Gab2 protein was completely depleted in the Gab2KO and DKO mice, indicating the successful depletion of Gab1 and Gab2 in the cardiomyocytes of DKO mice (Figure 2C).

DKO mice display dilated cardiomyopathic features accompanied by endocardial fibroelastosis. We performed gross morphological examination of the hearts of the 4 groups at 10 weeks of age because we did not find any morphological abnormalities in the hearts of Gab1CKO, Gab2KO, or DKO mice at birth (Supplemental Figure 5A). Although there was no morphological difference among Gab1CKO, Gab2KO, and control mice (Figure 3A), DKO mice exhibited significantly higher heart weight–to–body weight ratios

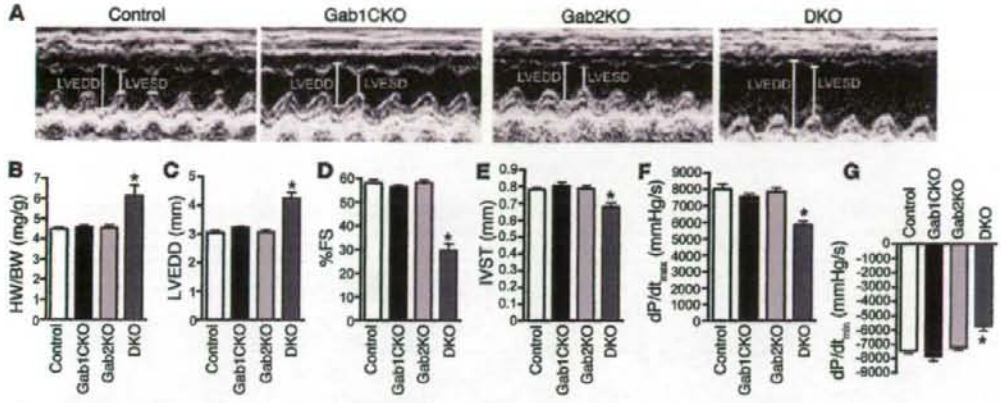

Figure 4

DKO mice exhibit dilated cardiomyopathic features. (**A**) Representative examples of M-mode echocardiographic images of LV from each group of mice at 10 weeks of age. LVEDD, LV end-diastolic dimension; LVESD, LV end-systolic dimension. (**B**) Heart weight/body weight (HW/BW) ratio of control mice (n = 9), Gab1CKO mice (n = 6), Gab2KO mice (n = 6), and DKO mice (n = 10) at 10 weeks of age. (**C**) LVEDD, (**D**) fractional shortening (%FS), and (**E**) interventricular septal thickness (IVST) of control mice (n = 8), Gab1CKO mice (n = 8), Gab2KO mice (n = 7), and DKO mice (n = 14) at 10 weeks of age. There were no significant differences in BW or heart rate among the 4 groups. (**F**) The maximum first derivative of LV pressure (LV dP/dt$_{max}$) and (**G**) the minimum first derivative of LV pressure (LV dP/dt$_{min}$) were obtained by catheterization of LV from right carotid artery in control mice (n = 7), Gab1CKO mice (n = 6), Gab2KO mice (n = 7), and DKO mice (n = 7) at 12 weeks of age. *P < 0.01 compared with all other genotypes.

than the other 3 groups without significant differences in body weight (Figure 3A and Figure 4B). Histological examination also demonstrated both left and right ventricular enlargement in DKO mice similar to DCM (Figure 3B).

A significant accumulation of elastic fibers and collagen was observed exclusively in the endocardium of DKO mice (Figure 3, B–F), while fibrotic replacement was not found in the interstitial spaces of the ventricles of DKO mice (Supplemental Figure 6, A and B). There was no significant increase in the number of apoptotic myocardial cells in the hearts of DKO mice compared with those of control mice (Supplemental Figure 7, A and B). The endocardial deposition of elastic fibers and collagen was not found in the neonates of DKO, but was found to some extent in all of the DKO mice after 3 weeks (Supplemental Figure 5A and data not shown). These endocardium-specific changes were coincident with the pathological features of endocardial fibroelastosis (EFE), the genetic causality of which has not been fully elucidated to date (37, 38). We further examined the vasculature in the heart by immunostaining with anti-vWF Ab. Intriguingly, we found abnormally dilated vessels positively stained with anti-vWF Ab exclusively in the LV of DKO mice but not in those of control, Gab1CKO, or Gab2KO mice (Figure 5A). These dilated vessels in DKO mice exhibited the impairment in recruitment of α-SMA–positive VSMCs (Figure 5, B and C). These findings indicate that the maintenance system for both endocardial and vascular endothelium might be disturbed in the DKO mouse hearts. Furthermore, EFE and increased abnormal vessels in the hearts of DKO mice were indirectly ascribed to the lack of Gab1 and Gab2 in the myocardium because there was no abnormality in the other 3 groups.

We assessed in vivo cardiac function by echocardiography and cardiac catheterization. Echocardiography revealed a significant increase in LV end-diastolic dimension (Figure 4, A and C), decreased fractional shortening (Figure 4, A and D), and decreased interventricular septal wall thickness (Figure 4E) in 10-week-old DKO mice compared with age-matched mice of the other 3 groups. Although we did not find a significant changes of LV end-diastolic dimension or fractional shortening between the DKO and control mice at 3 weeks of age, we did observe these changes after 6 weeks of age (Supplemental Figure 8, A and B). Consistent with the echocardiographic findings, cardiac catheterization at 12 weeks of age revealed a marked reduction of the maximum first derivative of LV pressure exclusively in DKO (Figure 4F), demonstrating a reduction in myocardial contractility of the DKO hearts. The accompanying reduction of the minimum first derivative of LV pressure in the DKO mouse hearts indicated the impairment of LV relaxation (Figure 4G). There were no significant differences in heart rate or LV peak pressure among the 4 groups (data not shown). This relaxation failure was supported by the electron microscopic findings. We noticed that sarcomere length was reduced in the DKO mouse hearts, which indicated the hypercontraction phenotype (39), although we could detect slight changes in the mitochondria of DKO mouse hearts (Supplemental Figure 7, C and D). In agreement with the reduced contractility and relaxation reflecting heart failure, the fetal cardiac gene program was reactivated, as evidenced by the significant increase in both *atrial natriuretic peptide* (*ANP*) and *skeletal α-actin* (*α-SKA*) mRNAs in DKO mice (Figure 6, A–C).

Approximately 70% of the DKO mice died, presumably of heart failure accompanied by pleural effusion, between 3 and 72 weeks of age (Figure 6D). We observed remarkably dilated ventricles in DKO mice that had died of heart failure (Supplemental Figure 5B, right panel). The other 3 groups of mice lived normally during the observation period of 500 days (Figure 6D). In agreement with this survival analysis, we did not observe any enlargement of the hearts of Gab1CKO and Gab2KO mice at 300 and 500 days of age. (Supplemental Figure 5B and data not shown). These data indicate that depletion of both Gab1 and Gab2 in the myocardium result in DCM-like phenotype accompanied by EFE.

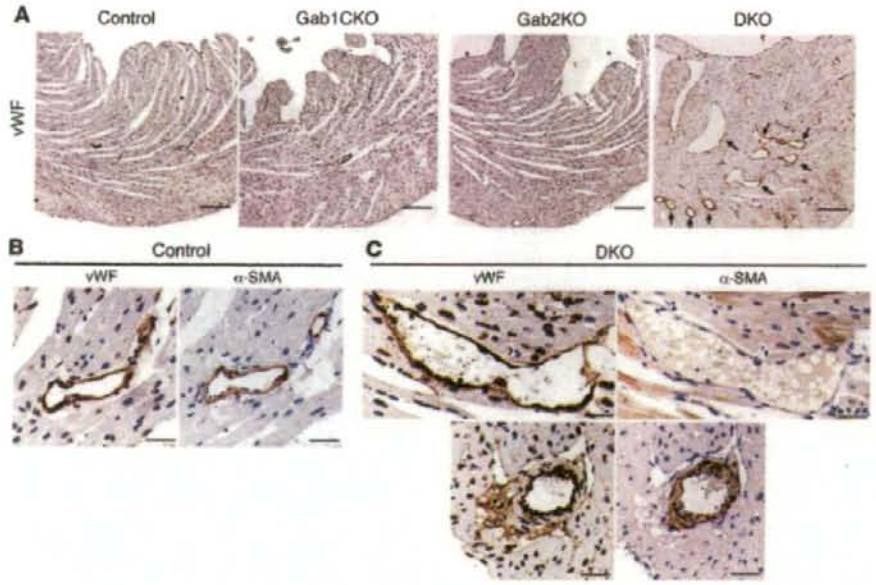

Figure 5

DKO mice display vascular abnormalities in the ventricles. (**A**) Heart sections from 4 groups of mice at 6 weeks of age were immunostained with anti-vWF Ab. vWF-positive, abnormally dilated vessels were observed in the left ventricles of DKO mice (arrows) but not in those of control, Gab1CKO, or Gab2KO mice. Representative photographs are shown. (**B** and **C**) Heart sections from control (**B**) and DKO (**C**) mice at 6 weeks of age were immunostained with anti-vWF and anti–α-SMA Abs. The abnormally dilated vessels in DKO mice were not surrounded by α-SMA–positive VSMCs in most cases (**C**, top panels), although vessels of normal diameter near the epicardium in DKO mice were surrounded by α-SMA–positive VSMCs (**C**, bottom panels) as observed in control mice (**B**). Representative images are shown. Scale bars: 200 μm (**A**); 20 μm (**B** and **C**).

Gab1 and Gab2 are required for NRG-1β/ErbB signaling in the heart. To determine requirements of Gab1 and Gab2 in NRG-1β–triggered signaling in the myocardium, we examined the activation of ERK and AKT after injection of NRG-1β. NRG-1β–induced activation of ERK and AKT was completely abrogated in DKO mice but not in the other 3 groups (Figure 7, A–C), suggesting a compensatory function of Gab1 and Gab2 in the heart. Consistently, tyrosine phosphorylation of Gab1 and subsequent association with SHP2 and p85 were observed in control and Gab2KO mice but not in Gab1CKO or DKO mice (Figure 7D). Tyrosine phosphorylation of Gab2 and subsequent association with SHP2 and p85 were conversely observed in control or Gab1CKO mice but not in Gab2KO or DKO mice (Figure 7E). Tyrosine phosphorylation of ErbB2 and ErbB4 was comparable among the 4 groups (Figure 7F). IGF-1– and HB-EGF–dependent activation of ERK and AKT were not affected in the hearts of DKO mice (Supplemental Figure 9, A and B). These data indicate that Gab1 and Gab2 are required exclusively for NRG-1β/ErbB signal-dependent activation of ERK and AKT in the heart.

Angiopoietin 1 upregulation induced by NRG-1β is impaired in Gab1/Gab2-deficient myocardium. Because we observed no cardiac abnormalities in Gab2KO mice, we determined that the primary cause of EFE and abnormal vessels in DKO mouse hearts was not the lack of Gab2 in endothelial cells. To identify the potential signal defect that caused EFE and malformed vessels downstream of the NRG-1β/ErbB–Gab1/Gab2 signaling pathway in the myocardium, we used microarrays to carry out a global survey of mRNA in control and DKO mice treated with or without NRG-1β for 8 hours. We found several transcripts that were upregulated by stimulation with NRG-1β in the hearts of control mice but not in those of DKO mice (Figure 8A). Among these transcripts presented in the cluster diagram, we considered thrombospondin 1 (TSP1) and angiopoietin 1 (Ang1) to be potential paracrine factors from myocardium and Eph receptor A4 (EphA4) to be important for the intercellular communication between cardiomyocytes and surrounding cells.

To address the pathogenesis of endocardial and vascular abnormalities observed in DKO mouse hearts, we focused on Ang1 because it has an important role in maturation of both vascular endothelium and endocardial endothelium in vivo (40–42). We confirmed by northern blot analysis that NRG-1β upregulated *Angl* mRNA in the hearts of control mice, but not DKO mice (Figure 8, B and C). NRG-1β consistently induced significant upregulation of *Angl* mRNA in cultured cardiomyocytes but not in noncardiomyocytes (Figure 8, D–F). In association with defective expression of Ang1, CD31-positive capillary density was significantly decreased in the LV of DKO mice compared with control (Figure 8, G and H). Taken together, these findings suggest that the lack of NRG-1β–induced upregulation of Ang1 might be one of the possible causes for pathogenesis of EFE and abnormal vasculatures in DKO mouse hearts.

Discussion

To our knowledge, the present study is the first to reveal the essential roles of Gab family proteins for NRG-1β/ErbB signaling pathway in the heart. Gab1 and Gab2 were markedly tyro-

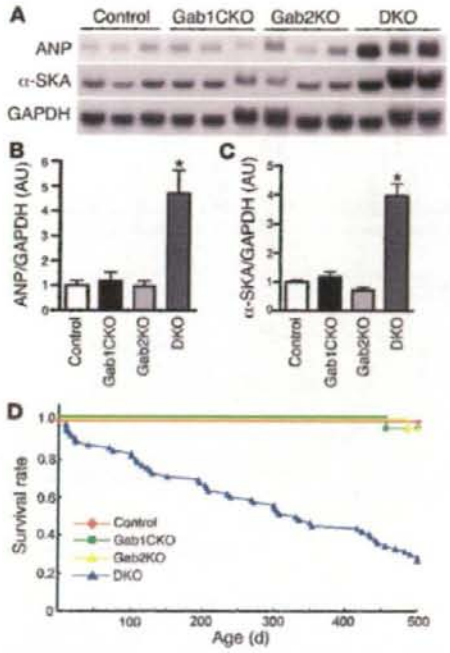

Figure 6
DKO mice die of heart failure. (**A**) Northern blot analyses of the hearts from control, Gab1CKO, Gab2KO, and DKO mice (n = 3 for each group) at 12–14 weeks of age showed the increased expression of mRNAs for *ANP* and α-*SKA* in DKO mice. *GAPDH* mRNA was also measured for sample loading control. (**B** and **C**) The relative levels of *ANP* and α-*SKA* mRNA (normalized to *GAPDH* mRNA levels) were quantified from 3 mouse hearts in each group. (*P < 0.01 compared with all other groups.) (**D**) Kaplan-Meier curves showing survival rate in control mice (n = 30), Gab1CKO mice (n = 30), Gab2KO mice (n = 30), and DKO mice (n = 66) mice by 500 days. The number of dead DKO mice was 48 (72.7%); P < 0.001 for DKO versus control, Gab1CKO, and Gab2KO mice by log-rank test.

sine phosphorylated in the myocardium after stimulation with NRG-1β among various growth factors and cytokines. Tyrosine-phosphorylated Gab1 and Gab2 subsequently associated with SHP2 and p85, resulting in strong activation of both ERK and AKT in the myocardium. NRG-1β–dependent activation of ERK and AKT was almost completely abrogated in the DKO mouse hearts. In agreement with NRG-1β–dependent downstream signaling defects, DKO mice displayed DCM-like phenotypes and EFE with aging. Interestingly, DKO mouse hearts also displayed abnormally dilated vessels with the loss of VSMCs. To address the mechanism for the abnormality in endocardial/vascular endothelium in DKO mouse hearts, we performed DNA microarray analysis and found several vasculature-regulating gene transcripts, such as Ang1, upregulated by NRG-1β in control, but not in DKO, mouse hearts. Thus, Gab family proteins mediate NRG-1β–dependent stabilization of endocardial/vascular endothelium through the paracrine system from cardiomyocytes in the heart.

Gab1 and Gab2 are specifically required for coordination of NRG-1β/ErbB–dependent signaling pathway in the myocardium. NRG-1β shed from endothelial cells activates ErbB2/ErbB4 heterodimer or ErbB4 homodimer on the cardiomyocytes (16, 17, 21). Consistent with this notion, we found that NRG-1β induced prominent tyrosine phosphorylation of Gab1 and Gab2 in cardiomyocytes but not in noncardiomyocytes. In addition, the cardiomyocyte-specific, high-MW isoform of Gab1 was tyrosine phosphorylated after stimulation with NRG-1β but not with other agonists including HB-EGF and EGF. It has been reported that HB-EGF–deficient mice develop heart failure (25, 26). Given that HB-EGF induced a much stronger tyrosine phosphorylation of Gab1 and Gab2 in noncardiomyocytes than in cardiomyocytes in our study and that valvular structures are developed from noncardiomyocytes (19), the heart failure observed in HB-EGF–deficient mice might have resulted from abnormal signaling in the development of the valvular apparatus. Therefore, the cardiac phenotypes observed in DKO mice were mainly ascribable to the defects of the NRG-1β/ErbB signaling pathway in the myocardium. Consistent with this, similar DCM-like phenotypes are found in cardiac-specific ErbB2- and ErbB4-deficient mice (29–31).

NRG-1β activates both ERK and PI3K/AKT pathways in cardiomyocytes in vitro, both of which have been implicated in modulation of cell survival and protein synthesis (21, 43). NRG-1β actually induced strong activation of ERK and AKT in the hearts of control, but not DKO, mice. This finding provides what we believe to be the first in vivo evidence that Gab1 and Gab2 are required for transmission of the NRG-1β/ErbB signal to downstream signaling pathways, ERK and AKT. DKO mice progressively developed DCM phenotypes, demonstrating clearly that Gab1 and Gab2 were essential for maintenance of myocardial function through transmission of NRG-1β/ErbB signaling pathway (Figure 9).

DKO mice also exhibited abnormal deposition of elastic fibers and collagen specifically in the endocardium, reminiscent of the pathological features observed in primary EFE. Clinically, primary EFE is found mainly in infants, children, and adolescents and is frequently accompanied by contractile deterioration similar to DCM. Although there have been some reports suggesting the heritable causality of primary EFE (37, 38), the precise pathogenetic mechanisms have not been elucidated to date. These DKO mice may provide the first mouse model of EFE. Further genetic analysis of cardiac-specific isoform of Gab1 will certainly contribute to our understanding of the pathogenesis of EFE.

DKO mouse hearts also displayed abnormal vasculatures as well as EFE. Microarray analysis enabled us to identify several transcripts that were upregulated by NRG-1β in the control hearts but not in DKO hearts. Among these transcripts selected in the cluster analysis, TSP1, EphA4, and Ang1 have been reported to be involved in the intercellular-dependent vascular regulation (40, 44, 45). Intriguingly, NRG-1β/ErbB2/ErbB4 signaling, Ang1/Tie2 signaling, VEGF/VEGFR2 signaling, and serotonin-mediated ($5\text{-}HT_{2B}$–mediated) signaling are required for the proper maturation of endocardium (16, 17, 40, 46, 47). Moreover, Ang1- or Tie2-deficient mice exhibit embryonic lethality accompanied by abnormally dilated vessels as well as defects in the endocardium (40, 42, 48). Furthermore, we demonstrated for the first time that postnatal cardiomyocytes are important Ang1-producing cells, whereas Ang1 has been believed to be mainly secreted from vascular mural cells such as pericytes and VSMCs (40, 41). Thus, we could pro-

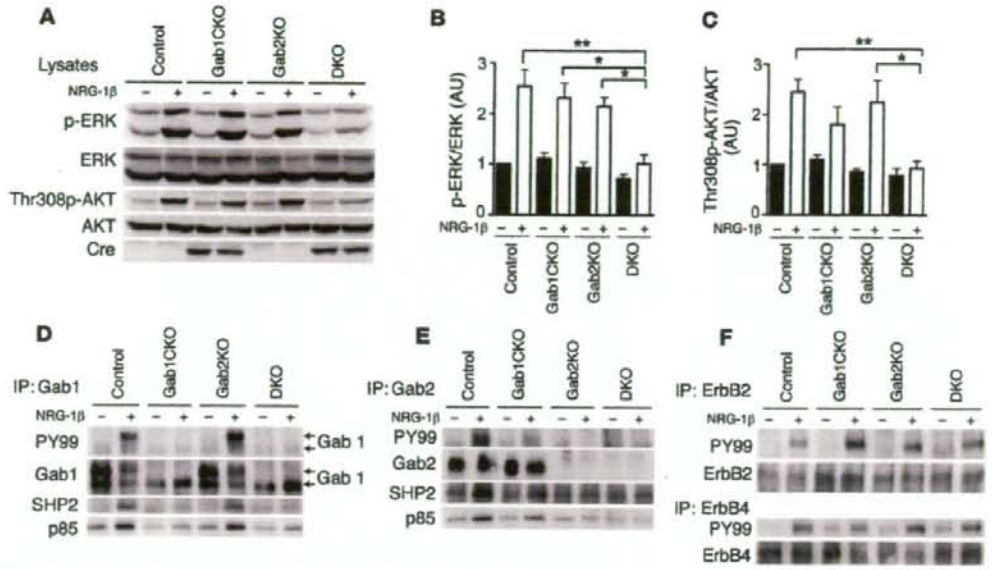

Figure 7

Gab1 and Gab2 are required for NRG-1β–dependent ERK and AKT activation in the heart. (**A**) NRG-1β–induced activation of ERK and AKT in the hearts from the indicated mice was assessed using phospho-specific Abs. Activation of ERK and AKT was exclusively attenuated in DKO hearts compared with the other 3 groups. Representative blots of 4 experiments are shown. (**B**) Phosphorylation of ERK was quantified against total ERK ($n = 4$). (**C**) Phosphorylation of AKT was quantified against total AKT ($n = 4$). $^*P < 0.05$, $^{**}P < 0.01$ for the indicated groups. Tyrosine phosphorylation of Gab1 (**D**) and Gab2 (**E**) and their association with SHP2 and p85 in hearts from the 4 groups of mice after injection with NRG-1β was examined as in Figure 1, A and B. Arrows in **D** denote the 2 isoforms of Gab1. (**F**) Tyrosine phosphorylation of ErbB2 (upper panels) and ErbB4 (lower panels) in hearts from the 4 groups were assessed at 5 minutes after NRG-1β injection. Tyrosine phosphorylation of ErbB receptors in the murine hearts upon NRG-1β stimulation was examined by IP with anti-ErbB2 or anti-ErbB4 Ab, followed by IB with the Abs indicated at the left.

pose that the defective expression of Ang1 might be involved in the pathogenesis of EFE and abnormal vessels in DKO hearts, though we cannot exclude the possibility that other vasculature-regulating genes, such as TSP1 and EphA4, play important roles in endocardial maintenance. Cardiac-specific gene ablation of Ang1 would be helpful to understand its importance in cardiomyocyte-endothelial cell interactions.

So far, it has been well established that NRG-1 functions as a cytoprotective growth factor in cardiomyocytes (17, 21, 43). Here, our findings propose a novel function of NRG-1; NRG-1 regulates vascular homeostasis through the paracrine expression of endothelium stabilization factors, such as Ang1, via Gab family proteins. Importantly, accumulating evidence has revealed that normal endothelial function is required for the maintenance of myocardial function (16). Collectively, Gab1 and Gab2 in the myocardium are essential for both maintenance of myocardial function and stabilization of capillary or endocardial endothelium through transmission of NRG-1β/ErbB signaling (Figure 9).

Methods

Materials. Anti–phospho-p44/p42 ERK (Thr202/Tyr204), anti–phospho-AKT (Thr308), and anti-AKT Abs were purchased from Cell Signaling Technology. The use of anti-Gab1 and anti-Gab2 serums in IP was described previously (13, 49). The Abs against Gab1, Gab2, and p85 used in IB analysis were from Millipore; Abs against antibody recognizing phospho-tyrosine (PY99), ERK1, ERK2, and SHP2 were from Santa Cruz Biotechnology Inc.; Abs against vWF and α-SMA were from Dako; the Ab against CD31 was from BD Biosciences — Pharmingen; and the Ab against Cre was from EMD Biosciences. Collagenase, Percoll, recombinant NRG-1β (NRG-1β EGF domain; sold as heregulin-β1), HGF, and PDGF-BB were from Sigma-Aldrich. HB-EGF and EGF were from R&D Systems. FGF2 was from EMD Biosciences. LIF was from Millipore. IGF-1 and erythropoietin were kindly provided by Astellas Pharma and Chugai Pharmaceutical Co., respectively.

Cell cultures. Primary cultures of neonatal rat cardiomyocytes were prepared from ventricles of 1- to 2-day-old Wistar rats (Kiwa Jikken Dobutsu) on Percoll gradient as described previously (32). Briefly, ventricles were isolated from neonatal rats and treated with trypsin and collagenase for 30 minutes at 37°C. Isolated cells were suspended in 58.5% Percoll in HBSS (20 mM HEPES, 116 mM NaCl, 12.5 mM NaH_2PO_4, 5.6 mM glucose, 5.4 mM KCl, 0.8 mM $MgSO_4$; pH 7.35) and added to the discontinuous gradient consisting of 40.5% and 58.5% Percoll in HBSS. After centrifugation at 1,400 *g* for 30 minutes at 15°C, the cardiomyocytes were collected from the interface of the discontinuous Percoll gradient and further enriched by preplating for 60 minutes on noncoated dishes. Unattached cells were cultured as cardiomyocytes in M-199 (Invitrogen) with 10% FBS. Attached cells were cultured as noncardiomyocytes in DMEM with 10% FBS. Immunocytochemical examination with anti-sarcomeric α-actinin Ab (Sigma-Aldrich) revealed that more than 95% cultured cells in the cardiomyocyte fraction were sarcomeric α-actinin–positive cardiomyocytes (data not shown). The population of noncardiomyocytes is described in the supplemental information.

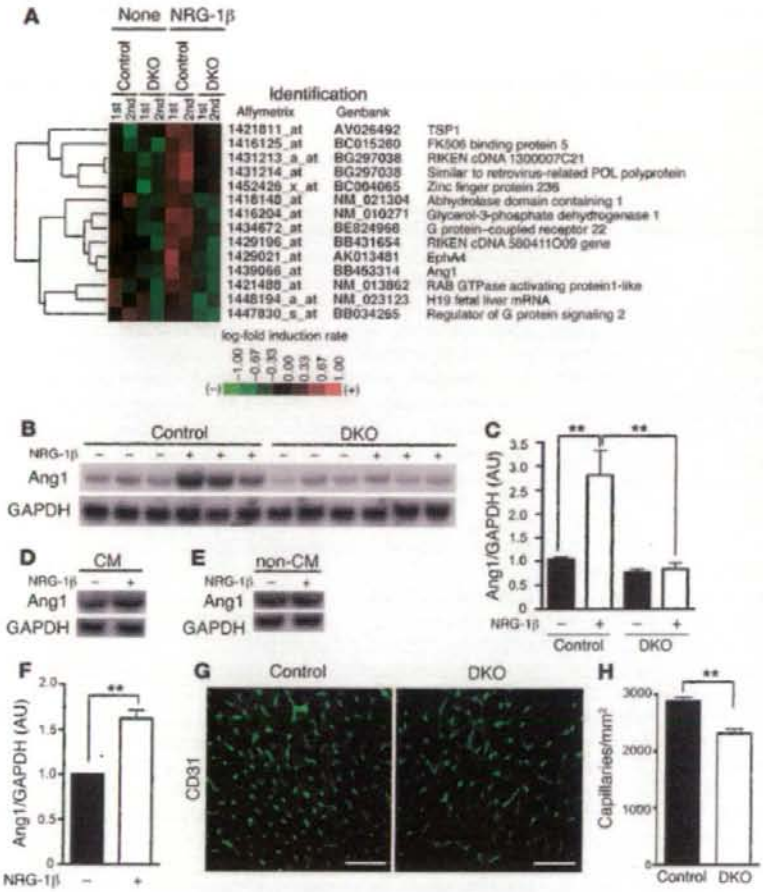

Figure 8

Gab1 and Gab2 are required for the NRG-1β–induced Ang1 upregulation and endothelial stabilization in the heart. (**A**) RNAs from the ventricles of control and DKO mice ($n = 3$ per group) were prepared 8 hours after injection with NRG-1β or vehicle. This preparation was performed twice. We used pooled RNAs from 3 mice and performed Affymetrix DNA microarrays independently 2 times (indicated as 1st and 2nd). Cluster analysis was performed of upregulated (red) and downregulated (green) genes in NRG-1β–treated control and DKO mice. Color intensity is relative to the median (black). (**B**) Northern blot analysis demonstrated the upregulation of *Ang1* mRNA in the hearts of control mice but not in those of DKO mice following injection with NRG-1β ($n = 3$ per group). *GAPDH* mRNA was checked for gel loading. (**C**) Quantitative analysis of *Ang1* mRNA (normalized to *GAPDH* mRNA) ($n = 3$ per group; $^{**}P < 0.01$ between the indicated groups). (**D** and **E**) Ang1 expression was upregulated in cardiomyocytes but not in noncardiomyocytes after stimulation with NRG-1β. (**F**) Quantitative analysis of *Ang1* mRNA normalized to *GAPDH* mRNA ($n = 4$; $^{**}P < 0.01$). (**G**) Cryosections of the hearts from control and DKO mice were immunostained with anti-CD31 Ab. Representative results are shown. Scale bars: 50 μm. (**H**) Capillary densities were counted from the number of capillaries per square millimeter. $^{**}P < 0.01$.

Biochemical analyses. Mice (body weight, approximately 20 g) were injected with following agonists: LIF (1×10^4 U), NRG-1β (5 μg), HB-EGF (5 μg), EGF (5 μg), FGF2 (2 μg), IGF-1 (5 μg), HGF (2 μg), PDGF-BB (5 μg), and erythropoietin (600 IU). Briefly, mice anesthetized by avertin were injected i.v. via the inferior vena cava with various growth factors and cytokines dissolved in 100 μl of normal saline. The hearts were isolated 5 minutes after injection and washed with ice-cold 4°C PBS. After removing both atria, the ventricles were snap-frozen in liquid nitrogen. The ventricles were homogenized in lysis buffer containing 50 mM HEPES, 100 mM sodium fluoride, 2 mM sodium orthovanadate, 4 mM EDTA, 1% Tween-20, 0.1% SDS, and a protease inhibitor cocktail Complete (Roche Applied Science) using a polytron homogenizer as described previously (50). The lysates were cleared by centrifugation at 17,000 *g* for 30 minutes. Protein concentration was measured with BCA protein assay kit (Pierce). Lysates of cultured cells were prepared essentially as described previously (13). After stimulation, cells were immediately lysed in ice-cold lysis buffer (20 mM Tris-HCl (pH 7.4), 150 mM NaCl, 1% NP-40, 1 mM sodium vanadate, 1 mM dithiothreitol, and a protease inhibitor cocktail Complete). The cleared lysates were subjected to IP and IB following standard procedures as described previously (13).

Creation of a conditional Gab1 mutant allele. Genomic DNA fragments of *Gab1* were isolated from a λ-FixII 129/Sv mouse strain genomic library, and a targeting construct was engineered using a triple-*loxP* system (provided by W. Reith, Department of Pathology and Immunology, University of Geneva Medical School, Geneva, Switzerland). We flanked exon 2, which encodes part of pleckstrin homology domain with 2 *loxP* sites (which codes for amino acids 25–123). The linearized construct DNA was introduced into R1 embryonic stem cells by electroporation. G418-resistant cell colonies were screened for homologous recombination by PCR, as reconfirmed by Southern blot analysis. Embryonic stem cell clones with a *loxP*-floxed exon 2 ($Gab1^{flox}$) without the TK-neo cassette were obtained by transient transfection with a pCre-Pac (provided by T. Yagi, Osaka University) (51). The engineered embryonic stem cells were injected into C57BL/6J blastocysts.

Generation of Gab1CKO and DKO mice. $Gab1^{flox}$ allele was generated in 129/Sv-C57BL/6J mixed background. The transgenic mice expressing Cre recombinase under the control of α-MHC promoter in C57BL/6J background (α-MHC–Cre mice) were generated as previously reported (35). $Gab1^{flox/flox}$ mice were crossed with α-MHC–Cre mice to generate Gab1CKO mice ($Gab1^{flox/flox}Gab2^{+/+}$α-*MHC-Cre(+)*). We had also previously created Gab2KO mice and reported that these mice are viable and display defects in mast cells (9, 11). We further crossed Gab1CKO mice with Gab2KO mice to create DKO mice ($Gab1^{flox/flox}Gab2^{-/-}$α-*MHC-Cre(+)*). PCR primers used for mouse genotyping are listed in the supplemental informarion. All mice

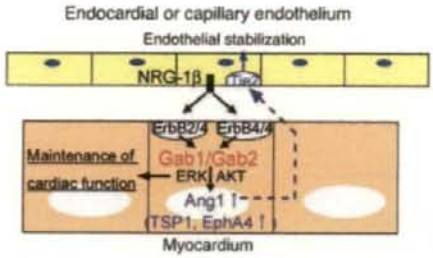

Figure 9
Schematic illustration of the roles of Gab family proteins in the myocardium. NRG-1β shed from the endocardial or capillary endothelium in the heart activates ErbB receptors on the myocardium, resulting in tyrosine phosphorylation of Gab family proteins and subsequent activation of ERK and AKT. NRG-1β/ErbB–Gab1/Gab2 signaling in the myocardium is directly required for postnatal maintenance of myocardial function. In addition, NRG-1β/ErbB–Gab1/Gab2 signaling indirectly contributes to postnatal stabilization of capillary or endocardial endothelium, possibly through Ang1 upregulation (dotted line).

were maintained on a 129/Sv-C57BL/6J mixed background. We housed all animals in a virus-free facility on a 12-hour light/12-hour dark cycle and fed them a standard mouse food. Animal experiments were approved by the National Cardiovascular Center Research Committee and were performed according to the institutional guidelines.

Histological analyses. Hearts from mice at indicated ages (see Results and Figure 3 legend) were fixed with 10% neutralized formalin, embedded in paraffin, and sectioned at 4 μm thickness. Masson trichrome and elastica van Gieson staining were performed on serial sections. To examine the capillary density, hearts of 4- to 6-week-old mice were fixed with 4% paraformaldehyde, cryoprotected with 20% sucrose, and frozen in OCT compound (Sakura). Cryosections (10 μm) were stained with rat monoclonal anti-CD31 Ab and FITC-conjugated secondary Ab. Paraffin sections of hearts from 4- to 6-week-old mice were immunostained with anti-vWF or anti–α-SMA Ab from the EnVision+ Kit (Dako) according to the manufacturer's instructions.

Physiological analyses. For echocardiography, male mice at the indicated ages were anesthetized with 2.5% avertin (Wako; 15 μl/g body weight). Echocardiography was performed using a Hewlett Packard Sonos 5500 Echocardiography System and a 15-MHz linear transducer. Ventricular dimensions were measured on M-mode images at least 3 times for each group of mice. For hemodynamic measurements, 12-week-old male mice were anesthetized with i.p. injection of urethane (750 mg/kg) and α-chloralose (50 mg/kg) dissolved in normal saline (52). The right common carotid artery was exposed via the midline incision. To allow the use of a physiologic closed-chest preparation, the LV was catheterized retrogradely from the carotid artery using a high-fidelity pressure transducer catheter (1.4 French; Millar Instruments) (53). The LV pressure was digitized, stored on the hard disk of a dedicated laboratory computer system, and analyzed with custom software.

Northern blot analysis. The probes for ANP, α-SKA, and GAPDH were kindly donated by K.R. Chien (Massachusetts General Hospital, Boston, Massachusetts, USA). Total RNA was prepared by TRIZOL reagent (Invitrogen) according to the manufacturer's instructions. RNAs from the ventricles of mouse hearts and cultured cardiomyocytes were subjected to Northern blot analyses against a panel of cDNA probes indicated in Results and the legends for Figures 6 and 8. Hybridization was performed using Quikhyb (Stratagene). Quantitative data were collected after normalizing the results to GAPDH.

Gene expression profiling using Affymetrix DNA microarrays. Gene expression in cardiac ventricular tissue was analyzed by Affymetrix microarray hybridization. Control and DKO male mice at 6 weeks of age were injected with 5 μg of NRG-1β or vehicle (normal saline) via tail vein. The ventricles were isolated at 8 hours after injection and subjected to extraction of total RNA using TRIZOL reagent. We pooled total RNA from 3 mouse ventricles for each group and subjected to the microarray hybridization as described previously (54). Preparation of cRNA and hybridization of probe on arrays were performed according to the manufacturer's instructions (Affymetrix). Each array experiment was performed in duplicate. FileMaker Pro 8.0 software was used to analyze genes that demonstrated identical patterns in 2 independent microarray experiments. Data were analyzed according to the minimum information about a microarray experiment (MIAME) rule. Annotation of the probe numbers and targeted sequences are shown on the Affymetrix website (https://www.affymetrix.com/site/login/login.affx).

Statistics. All data are expressed as mean ± SEM. Differences among multiple groups were compared by 1-way ANOVA followed by a post-hoc comparison using Scheffe's method. The 2-tailed Student's *t* test was used to analyze differences between 2 groups. $P < 0.05$ was considered statistically significant. Survival curves were generated using Kaplan-Meier method, and significance was evaluated using the log-rank test.

Acknowledgments

This work was supported in part by grants from the Ministry of Education, Culture, Sports, Science, and Technology of Japan (to Y. Nakaoka and N. Mochizuki); the Ministry of Health, Labour, and Welfare of Japan (to N. Mochizuki); the Program for the Promotion of Fundamental Studies in Health Sciences of the National Institute of Biomedical Innovation (to T. Minami, T. Kodama, and N. Mochizuki); the Japan Heart Foundation (Novartis Grant for Research Award on Molecular and Cellular Cardiology, to Y. Nakaoka); the Mitsubishi Pharma Research Foundation (to Y. Nakaoka); and the Uehara Memorial Foundation (to Y. Nakaoka). We thank Y. Matsuura, M. Yoshida, M. Miyabayashi, M. Maeoka, Y. Ohba, M. Sato, K. Sako, and K. Shioya for their technical assistance; S. Higashiyama, O. Nakagawa, and O. Ohara for helpful comments; K. Komamura for advice on echocardiography; and W.W. Hall and K. Yamauchi-Takihara for critical reading of the manuscript.

Received for publication October 16, 2006, and accepted in revised form April 10, 2007.

Address correspondence to: Naoki Mochizuki, Department of Structural Analysis, National Cardiovascular Center Research Institute, 5-7-1 Fujishirodai, Suita, Osaka 565-8565, Japan. Phone: 81-6-6833-5012, ext. 2508; Fax: 81-6-6835-5461; E-mail: nmochizu@ri.ncvc.go.jp. Or to: Yoshikazu Nakaoka: Department of Cardiovascular Medicine, Osaka University Graduate School of Medicine, 2-2, Yamada-oka, Suita, Osaka 565-0871, Japan. Phone: 81-6-6879-3835; Fax: 81-6-6879-3839; E-mail: ynakaoka@imed3.med.osaka-u.ac.jp.

Y. Nakaoka's present address is: Department of Cardiovascular Medicine, Osaka University Graduate School of Medicine, Osaka, Japan.

Hisao Hirota is deceased.